

Chapter 1

Quantum Chromodynamics

Thomas Schäfer

Abstract We present a brief introduction to QCD, the QCD phase diagram, and non-equilibrium phenomena in QCD. We emphasize aspects of the theory that can be addressed using computational methods, in particular euclidean path integral Monte Carlo, fluid dynamics, kinetic theory, classical field theory and holographic duality.

1.1 Introduction

The goal of this chapter is to provide a brief summary of Quantum Chromodynamics (QCD) and the QCD phase diagram, and to give an introduction to computational methods that are being used to study different aspects of QCD. Quantum Chromodynamics is a remarkable theory in many respects. QCD is an almost parameter free theory. Indeed, in the context of nuclear physics QCD is completely characterized by the masses of the up, down, and strange quark, and a reasonable caricature of nuclear physics emerges in the even simpler case in which the up and down quark are taken to be massless, and the strange quark is infinitely heavy. QCD nevertheless accounts for the incredible richness of the phase diagram of strongly interacting matter. QCD describes finite nuclei, normal and superfluid states of nuclear matter, color superconductors, hadronic gases, quark gluon plasma, and many other states. This rich variety of states is reflected in the large number of computational methods that have been brought to bear on problems in QCD. This includes a large number of methods for the structure and excitations of finite Fermi systems, quantum Monte Carlo methods, and a variety of tools for equilibrium and non-equilibrium statistical mechanics.

The bulk of this book is devoted to the study of few and many nucleon systems. Summarizing everything else in one brief chapter is obviously out of the question, both because of limitations of space and because of my limited expertise. I will therefore be very selective, and focus on a number of very simple yet powerful ideas. This reflects, in part, my background, which is not primarily in computational physics. It also reflects my conviction that progress in computational physics is unfortunately often reflected in increasingly complicated codes that obscure the simplicity of the underlying methods.

Thomas Schäfer

Department of Physics, North Carolina State University, Raleigh, NC 27695, USA, e-mail: tmschaef@ncsu.edu

1.2 Path integrals and the Metropolis algorithm

Consider a simple quantum mechanical problem, the motion of a particle in a one-dimensional potential. In order to be specific I will focus on the double well potential $V(x) = \lambda(x^2 - \eta^2)^2$, where η and λ are parameters. The Hamiltonian is

$$H = \frac{p^2}{2m} + \lambda(x^2 - \eta^2)^2. \quad (1.1)$$

Using a change of variables I can set $2m = \lambda = 1$. This implies that there is only one physical parameter in this problem, the barrier separation η . The regime $\eta \gg 1$ corresponds to the limit in which the system has two almost degenerate minima that are split by semi-classical tunneling events. The energy eigenstates and wave functions are solutions of the eigenvalue problem $H|n\rangle = |n\rangle E_n$. Once the eigenstates are known I can compute all possible correlation functions

$$\Pi_n(t_1, t_2, \dots, t_n) = \langle 0|x(t_1)x(t_2)\dots x(t_n)|0\rangle, \quad (1.2)$$

by inserting complete sets of states. An alternative to the Hamiltonian formulation of the problem is the Feynman path integral [1]. The path integral for the anharmonic oscillator is given by

$$\langle x_1|e^{-iHt_f}|x_0\rangle = \int_{x(0)=x_0}^{x(t_f)=x_1} \mathcal{D}x e^{iS}, \quad S = \int_0^{t_f} dt \left(\frac{1}{4}\dot{x}^4 - (x^2 - \eta^2)^2 \right). \quad (1.3)$$

This expression contains a rapidly oscillating phase factor e^{iS} , which prohibits any direct numerical attempt at computing the path integral. The standard approach is based on analytic continuation to imaginary time $\tau = it$. This is also referred to as Euclidean time, because the Minkowski interval $dx^2 - dt^2$ turns into the Euclidean expression $dx^2 + d\tau^2$. In the following I will consider the euclidean partition function

$$Z(T) = \int \mathcal{D}x e^{-S_E}, \quad S_E = \int_0^\beta d\tau \left(\frac{1}{4}\dot{x}^4 + (x^2 - \eta^2)^2 \right), \quad (1.4)$$

where $\beta = 1/T$ is the inverse temperature and we assume periodic boundary conditions $x(0) = x(\beta)$. To see that equ. (1.4) is indeed the partition function we can use equ. (1.3) to express the path integral in terms of the eigenvalues of the Hamiltonian, $Z(T) = \sum_n \exp(-E_n/T)$. In the following I will describe numerical simulations using a discretized version of the euclidean action. For this purpose I discretize the euclidean time coordinate $\tau_j = ja, i = 1, \dots, n$ where $a = \beta/n$ is the length of time interval. The discretized action is given by

$$S = \sum_{i=1}^n \left\{ \frac{1}{4a} (x_i - x_{i-1})^2 + a(x_i^2 - \eta^2)^2 \right\}, \quad (1.5)$$

where $x_i = x(\tau_i)$. I consider periodic boundary conditions $x_0 = x_n$. The discretized euclidean path integral is formally equivalent to the partition function of a statistical system of (continuous) "spins" x_i arranged on a one-dimensional lattice. This statistical system can be studied using standard Monte-Carlo sampling methods. In the following I will use the Metropolis algorithm [2]. Detailed numerical studies of the euclidean path integral can be found in [3–6].

The Metropolis method generates an ensemble of configurations $\{x_i\}^{(k)}$ where $i = 1, \dots, n$ labels the lattice points and $k = 1, \dots, N_{conf}$ labels the configurations. Quantum mechanical averages are computed by averaging observables over many configurations,

$$\langle \mathcal{O} \rangle = \lim_{N_{conf} \rightarrow \infty} \frac{1}{N_{conf}} \sum_{k=1}^{N_{conf}} \mathcal{O}^{(k)} \quad (1.6)$$

where $\mathcal{O}^{(k)}$ is the value of the classical observable \mathcal{O} in the configuration $\{x_i\}^{(k)}$. The configurations are generated using Metropolis updates $\{x_i\}^{(k)} \rightarrow \{x_i\}^{(k+1)}$. The update consists of a sweep through the lattice during which a trial update $x_i^{(k+1)} = x_i^{(k)} + \delta x$ is performed for every lattice site. Here, δx is a random number. The trial update is accepted with probability

$$P\left(x_i^{(k)} \rightarrow x_i^{(k+1)}\right) = \min\{\exp(-\Delta S), 1\}, \quad (1.7)$$

where ΔS is the change in the action equ. (1.5). This ensures that the configurations $\{x_i\}^{(k)}$ are distributed according to the ‘‘Boltzmann’’ distribution $\exp(-S)$. The distribution of δx is arbitrary as long as the trial update is micro-reversible, i. e. is equally likely to change $x_i^{(k)}$ to $x_i^{(k+1)}$ and back. The initial configuration is arbitrary. In order to study equilibration it is useful to compare an ordered (cold) start with $\{x_i\}^{(0)} = \{\eta\}$ to a disordered (hot) start $\{x_i\}^{(0)} = \{r_i\}$, where r_i is a random variable.

The advantage of the Metropolis algorithm is its simplicity and robustness. The only parameter to adjust is the distribution of δx . A simple choice is to take δx to be a Gaussian random number, and choose the width of the distribution so that the average acceptance rate for the trial updates is around 50%. Fluctuations of \mathcal{O} provide an estimate in the error of $\langle \mathcal{O} \rangle$. The uncertainty is given by

$$\Delta \langle \mathcal{O} \rangle = \sqrt{\frac{\langle \mathcal{O}^2 \rangle - \langle \mathcal{O} \rangle^2}{N_{conf}}}. \quad (1.8)$$

This requires some care, because the error estimate is based on the assumption that the configurations are statistically independent. In practice this can be monitored by computing the auto-correlation ‘‘time’’ in successive measurements $\mathcal{O}(\{x_i\}^{(k)})$.

I have written a simple fortran code that implements the Metropolis algorithm for euclidean path integrals [6]. The most important part of that code is a sweep through the lattice with a Metropolis update on every site τ_j :

```
do j=1,n-1

    nhit = nhit+1

    xpm = (x(j)-x(j-1))/a
    xpp = (x(j+1)-x(j))/a
    t = 1.0/4.0*(xpm**2+xpp**2)
    v = (x(j)**2-f**2)**2
    sold = a*(t+v)

    xnew = x(j) + delx*(2.0*ran2(iseed)-1.0)

    xpm = (xnew-x(j-1))/a
    xpp = (x(j+1)-xnew)/a
    t = 1.0/4.0*(xpm**2+xpp**2)
    v = (xnew**2-f**2)**2
    snew = a*(t+v)
    dels = snew-sold

    p = ran2(iseed)
    if (exp(-dels) .gt. p) then
        x(j) = xnew
        nacc = nacc + 1
```

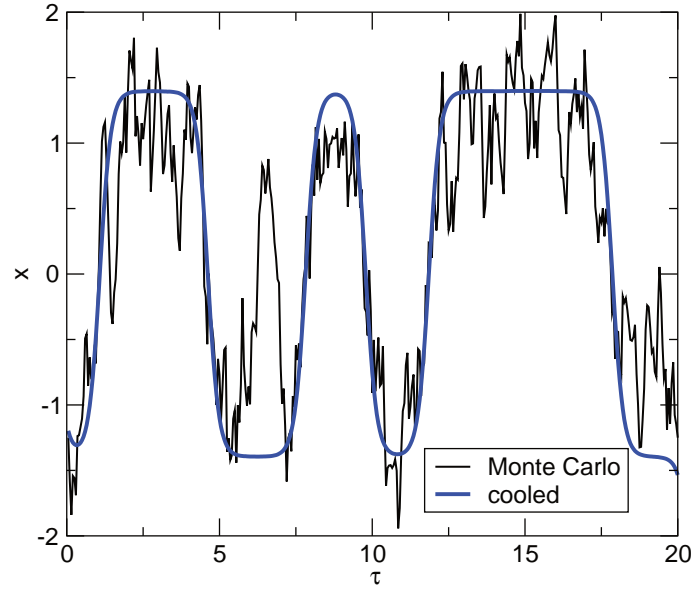


Fig. 1.1 Typical euclidean path obtained in a Monte Carlo simulation of the discretized euclidean action of the double well potential for $\eta = 1.4$. The lattice spacing in the euclidean time direction is $a = 0.05$ and the total number of lattice points is $N_\tau = 800$. The green curve shows the corresponding smooth path obtained by running 100 cooling sweeps on the original path.

endif

enddo

Here, $sold$ is the local action corresponding to the initial value of $x(j)$, and $snew$ is the action after the trial update. The trial update is accepted if $\exp(-dels)$ is greater than the random variable p . The function $ran2()$ generates a random number between 0 and 1, and $nacc/nhit$ measures the acceptance rate. A typical path is shown in Fig. 1.1. An important feature of the paths in the double well potential is the presence of tunneling events. Indeed, in the semi-classical regime $\eta \gg 1$, a typical path can be understood as Gaussian fluctuations superimposed on a series of tunneling events (instantons).

The path integral method does not provide direct access to the eigenvalues of the Hamiltonian, but it can be used to compute imaginary time correlation functions

$$\Pi_n^E(\tau_1, \dots, \tau_n) = \langle x(\tau_1) \dots x(\tau_n) \rangle. \quad (1.9)$$

Note that the average is carried out with respect to the partition function in equ. (1.4). In the limit $\beta \rightarrow \infty$ this corresponds to the ground state expectation value. A very important observable is the two-point function $\Pi^E(\tau) \equiv \Pi_2^E(0, \tau)$. The euclidean correlation function is related to the eigenstates of the Hamiltonian via a spectral representation. This representation is obtained by inserting a complete set of states into equ. (1.9). The result is

$$\Pi^E(\tau) = \sum_n |\langle 0|x|n\rangle|^2 \exp(-(E_n - E_0)\tau), \quad (1.10)$$

where E_n is the energy of the state $|n\rangle$. This can be written as

$$\Pi^E(\tau) = \int dE \rho(E) \exp(-(E - E_0)\tau), \quad (1.11)$$

where $\rho(E)$ is the spectral function. In the case of the double well potential there are only bound states and the spectral function is a sum of delta-functions. Equ. (1.10) shows that the euclidean correlation function is easy to construct once the energy eigenvalues and eigenfunctions are known. The inverse problem is well defined in principle, but numerically much more difficult. The excitation energy of the first excited state $\Delta E_1 = E_1 - E_0$ is easy to extract from the exponential decay of the two-point functions, but higher states are more difficult to compute. A technique for determining the spectral function from euclidean correlation functions is the maximum entropy image reconstruction method, see [7, 8].

The calculation of correlation functions in a Monte Carlo simulation is very straightforward. All I need to do is multiply the values of $x(\tau_i)$ for a given path, and then average over all paths:

```
do ic=1,nc
    ncor = ncor + 1
    ip0 = int( (n-np)*ran2(iseed) )
    x0 = x(ip0)
    do ip=1,np
        x1 = x(ip0+ip)
        xcor = x0*x1
        x2cor= xcor**2
        xcor_sum(ip) = xcor_sum(ip) + xcor
        xcor2_sum(ip) = xcor2_sum(ip) + xcor**2
    enddo
enddo
```

The advantages of this method are that it is extremely robust, that it requires no knowledge (or preconceived notion) of what the wave function looks like, and that it can explore a very complicated configuration space. On the other hand, in the case of one-dimensional quantum mechanics, the Metropolis method is very inefficient. Using direct diagonalization in a finite basis it is not difficult to compute the energies of the first several states in the potential in equ. (1.1) with very high accuracy, $\Delta E/E_0 \sim O(10^{-6})$ or better. On the other hand, using the Monte Carlo method, it is quite difficult to achieve an accuracy of $O(10^{-2})$ for observable other than $(E_1 - E_0)/E_0$. The advantage of the Monte Carlo method is that the computational cost scales much more favorably in high dimensional systems, such as quantum mechanics of many particles, or quantum field theory.

The Monte Carlo method also does not directly provide the ground state energy, or the partition function and free energy at finite temperature. In quantum mechanics we can compute the ground state energy from the expectation value of the Hamiltonian $\langle H \rangle = \langle T + V \rangle$ in the limit $\beta \rightarrow \infty$. The expectation value of the kinetic energy is singular as $a \rightarrow 0$, but this problem can be overcome by using the Virial theorem

$$\langle H \rangle = \left\langle \frac{x}{2} V' + V \right\rangle. \quad (1.12)$$

There is no simple analog of this method in quantum field theory. A method for computing the free energy which does generalize to quantum field theory is the adiabatic switching technique. The idea is to start from a reference system for which the free energy is known and calculate the free energy difference to the real system using Monte Carlo methods. For this purpose I write the action as

$$S_\alpha = S_0 + \alpha \Delta S, \quad (1.13)$$

where S_0 is the action of the reference system, ΔS is defined by $\Delta S = S - S_0$ where S is the full action, and α can be viewed as a coupling constant. The action S_α interpolates between the physical system for $\alpha = 1$ and the reference system for $\alpha = 0$. Integrating the relation $\partial \log Z(\alpha) / (\partial \alpha) = -\langle \Delta S \rangle_\alpha$ I find

$$\log(Z(\alpha=1)) = \log(Z(\alpha=0)) - \int_0^1 d\alpha' \langle \Delta S \rangle_{\alpha'} , \quad (1.14)$$

where $\langle \cdot \rangle_\alpha$ is computed using the action S_α . In the case of the anharmonic oscillator it is natural to use the harmonic oscillator as a reference system. In that case the reference partition function is

$$Z(\alpha=0) = \sum_n \exp(-\beta E_n^0) = \frac{\exp(-\beta \omega_0/2)}{1 - \exp(-\beta \omega_0)} , \quad (1.15)$$

where ω_0 is the oscillator constant. Note that the free energy $F = T \log(Z)$ of the anharmonic oscillator should be independent of the reference frequency ω_0 . The integral over the coupling constant α can be calculated in a Monte Carlo simulation by slowly changing α from 0 to 1 during the simulation. Free energy calculations of this type play an important role in quantum chemistry, and more efficient methods for determining ΔF have been developed [9].

1.3 Quantumchromodynamics

1.3.1 QCD at zero temperature and density

The rich phenomenology of strong interacting matter is encoded in a deceptively simple Lagrangian. The fundamental fields in the Lagrangian are quark fields $q_{\alpha f}^c$ and gluon fields A_μ^a . Here, $\alpha = 1, \dots, 4$ is a Dirac spinor index, $c = 1, \dots, N_c$ with $N_c = 3$ is a color index, and $f = up, down, strange, charm, bottom, top$ is a flavor index. Interactions in QCD are governed by the color degrees of freedom. The gluon field A_μ^a is a vector field labeled by an index $a = 1, \dots, N_c^2 - 1$ in the adjoint representation. The $N_c^2 - 1$ multiplet of gluon fields can be used to construct a matrix valued field $A_\mu = A_\mu^a \frac{\lambda^a}{2}$, where λ^a is a set of traceless, Hermitian, $N_c \times N_c$ matrices. The QCD Lagrangian is

$$\mathcal{L} = -\frac{1}{4} G_{\mu\nu}^a G_{\mu\nu}^a + \sum_f^{N_f} \bar{q}_f (i\gamma^\mu D_\mu - m_f) q_f , \quad (1.16)$$

where $G_{\mu\nu}^a$ is the QCD field strength tensor defined by

$$G_{\mu\nu}^a = \partial_\mu A_\nu^a - \partial_\nu A_\mu^a + g f^{abc} A_\mu^b A_\nu^c , \quad (1.17)$$

and $f^{abc} = 4i \text{Tr}([\lambda^a, \lambda^b] \lambda^c)$ are the $SU(N_c)$ structure constants. The action of the covariant derivative on the quark fields is

$$iD_\mu q = \left(i\partial_\mu + g A_\mu^a \frac{\lambda^a}{2} \right) q , \quad (1.18)$$

and m_f is the mass of the quarks. The terms in equ. (1.16) describe the interaction between quarks and gluons, as well as nonlinear three and four-gluon interactions. Note that, except for the number of flavors and their masses, the structure of the QCD Lagrangian is completely fixed by the local $SU(N_c)$ color symmetry.

A natural starting point for studying the phase diagram of hadronic matter is to consider the light flavors (up, down, and strange) as approximately massless, and the heavy flavors (charm, bottom, top) as infinitely massive. In this limit the QCD Lagrangian is completely characterized by two integer valued parameters, the number of colors $N_c = 3$ and flavors $N_f = 3$, and a single dimensionless coupling constant g . Quantum fluctuations cause the coupling constant to become scale dependent [10, 11]. At one-loop order the running coupling constant is

$$g^2(q^2) = \frac{16\pi^2}{b_0 \log(q^2/\Lambda_{QCD}^2)}, \quad b_0 = \frac{11}{3}N_c - \frac{2}{3}N_f, \quad (1.19)$$

where q is a characteristic momentum and N_f is the number of active flavors. The scale dependence of the coupling implies that, as a quantum theory, QCD is not governed by a dimensionless coupling but by a dimensionful scale, the QCD scale parameter Λ_{QCD} . This phenomenon is known as dimensional transmutation [12].

A crucial aspect of the scale dependence of the coupling in QCD is that the effective interaction decreases as the energy or momentum scale is increased. This feature of QCD is called asymptotic freedom [10, 11]. It implies that high energy interactions can be analyzed using perturbative QCD. The flip side of asymptotic freedom is anti-screening, or confinement: The effective interaction between quarks increases with distance, and quarks are permanently confined into hadrons. The absence of colored states in the spectrum implies that the use of perturbation theory is subtle, even at high energy. Quantities that can be computed perturbatively either involve a sum over many hadronic states, or allow for a factorization of perturbative interactions and non-perturbative matrix elements.

If quarks are massless then QCD observables are dimensionless ratios like m_p/Λ_{QCD} , where m_p is the mass of the proton. This implies that the QCD scale is not a parameter of the theory, but reflects a choice of units. In the real world QCD is part of the standard model, quarks acquire masses by electroweak symmetry breaking, and the QCD scale is fixed by value of the coupling constant at the weak scale. Experiments determine the value of the QCD fine structure constant $\alpha_s = g^2/(4\pi)$ at the position of the Z boson pole, $\alpha_s(m_z) = 0.1184 \pm 0.0007$ [13]. The numerical value of Λ_{QCD} depends on the renormalization scheme used in computing quantum corrections to the coupling constant. Physical observables, as well as the value of b_0 , are independent of this choice. In the modified minimal subtraction (\overline{MS}) scheme the scale parameter is $\Lambda_{QCD} \simeq 200$ MeV [13].

A schematic phase diagram of QCD is shown in Fig. 1.2. In this figure I show the phases of strongly interacting matter as a function of the temperature T and the baryon chemical potential μ . The chemical potential μ controls the baryon density ρ , defined as 1/3 times the number density of quarks minus the number density of anti-quarks. In the following I will explain that the basic structure of the phase diagram is determined by asymptotic freedom and the symmetries of QCD. For more detailed reviews see [14–16].

At small temperature and chemical potential the interaction between quarks is dominated by large distances and the effective coupling is strong. This implies that quarks and gluons are permanently confined in color singlet hadrons, with masses of order Λ_{QCD} . The proton, for example, has a mass of $m_p = 935$ MeV. A simplistic view of the structure of the proton is that it is a bound state of three constituent quarks with effective masses $m_Q \simeq m_p/3 \simeq \Lambda_{QCD}$. These masses should be compared to the bare up and down quark masses which are of the order 10 MeV.

As a consequence of strong interactions between virtual quarks and anti-quarks in the QCD ground state a vacuum condensate of $\bar{q}q$ pairs is generated, $\langle \bar{q}q \rangle \simeq -\Lambda_{QCD}^3$ [17–19]. This vacuum expectation value spontaneously breaks the approximate chiral $SU(3)_L \times SU(3)_R$ flavor symmetry of the QCD Lagrangian down to its diagonal subgroup, the flavor symmetry $SU(3)_V$. Spontaneous chiral symmetry breaking implies the existence of Goldstone bosons, massless modes with the quantum numbers of the generators of the broken axial symmetry $SU(3)_A$. The

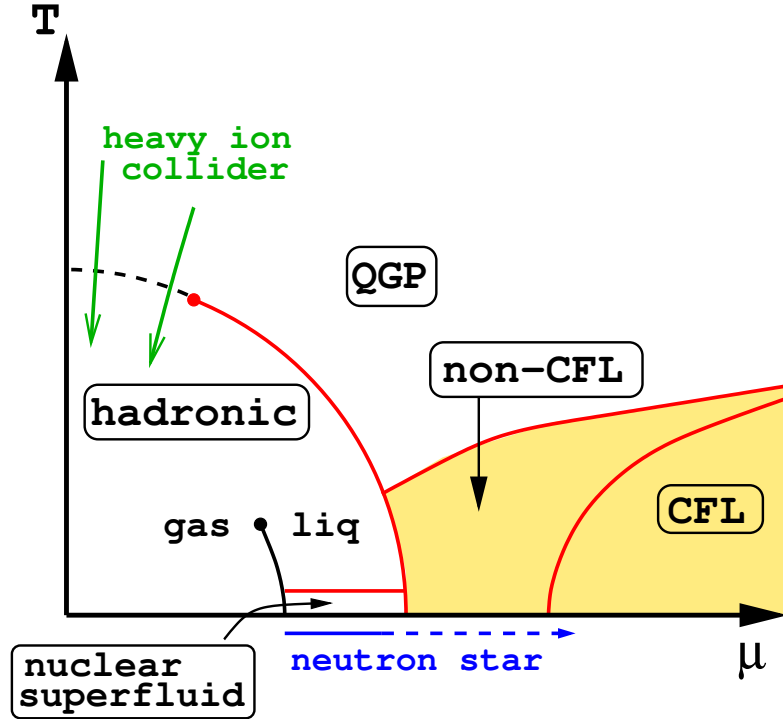


Fig. 1.2 Schematic phase diagram of QCD as a function of temperature T and baryon chemical potential μ . The quark gluon plasma phase is labeled QGP, and CFL refers to the color superconducting phase that is predicted to occur at asymptotically large chemical potential. The critical endpoints of the chiral and nuclear liquid-gas phase transitions, are denoted by red and black points, respectively. The chiral pseudo-critical line associated with the crossover transition at low temperature is shown as a dashed line. The green arrows indicate the regions of the phase diagram that can be studied by the experimental heavy ion programs at RHIC and the LHC.

corresponding excitations in the spectrum of QCD are the π , K and η mesons. The $SU(3)_L \times SU(3)_R$ symmetry is explicitly broken by quark masses, and the mass of the charged pion is $m_\pi = 139$ MeV. This scale can be compared to the mass of the lightest non-Goldstone particle, the rho meson, which has a mass $m_\rho = 770$ MeV.

At low energy Goldstone bosons can be described in terms of an effective field theory in which composite π , K and η particles are treated as fundamental fields. The Goldstone boson field can be parametrized by unitary matrices

$$\Sigma = \exp(i\lambda^a \phi^a / f_\pi), \quad (1.20)$$

where λ^a are the Gell-Mann matrices for $SU(3)$ flavor and $f_\pi = 93$ MeV is the pion decay constant. For example, $\pi^0 = \phi^3$ and $\pi^\pm = (\phi_1 \pm i\phi_2)/2$ describe the neutral and charged pion. Other components of ϕ^a describe the neutral and charged kaons, as well as the eta. The eta prime, which is the $SU(3)_F$ singlet meson, acquires a large mass because of the axial anomaly, and is not a Goldstone boson. The axial anomaly refers to the fact that the flavor singlet axial current, which is conserved in massless QCD at the classical level, is not conserved if quantum effects are taken into account. The divergence of the axial current $A_\mu = \bar{q}\gamma_\mu\gamma_5 q$ is

$$\partial_\mu A^\mu = \frac{g^2 N_f}{32\pi^2} \epsilon^{\mu\nu\alpha\beta} G_{\mu\nu}^a G_{\alpha\beta}^a. \quad (1.21)$$

The right hand side is the topological charge density, which I will discuss in more detail in Sect. 1.4.3.

At low energy the effective Lagrangian for the chiral field can be organized as a derivative expansion in gradients of Σ . Higher derivative terms describe interactions that scale as either the momentum or the energy of the Goldstone boson. Since Goldstone bosons are approximately massless, the energy is of the same order of magnitude as the momentum. We will see that the expansion parameter is $p/(4\pi f_\pi)$. At leading order in (∂/f_π) there is only one possible term which is consistent with chiral symmetry, Lorentz invariance and the discrete symmetries C, P, T . This is the Lagrangian of the non-linear sigma model

$$\mathcal{L} = \frac{f_\pi^2}{4} \text{Tr} [\partial_\mu \Sigma \partial^\mu \Sigma^\dagger] + [B \text{Tr}(M \Sigma^\dagger) + h.c.] + \dots, \quad (1.22)$$

where the term proportional to B takes into account explicit symmetry breaking. Here, $M = \text{diag}(m_u, m_d, m_s)$ is the quark mass matrix and B is a low energy constant that I will fix below.

First, I will show that the parameter f_π controls the pion decay amplitude. For this purpose I have to gauge the weak $SU(2)_L$ symmetry of the non-linear sigma model. As usual, this is achieved by promoting the derivative to a gauge covariant operator $\nabla_\mu \Sigma = \partial_\mu \Sigma + ig_w W_\mu \Sigma$ where W_μ is the charged weak gauge boson and g_w is the weak coupling constant. The gauged non-linear sigma model gives a pion- W boson interaction

$$\mathcal{L} = g_w f_\pi W_\mu^\pm \partial^\mu \pi^\mp. \quad (1.23)$$

This term contributes to the amplitude \mathcal{A} for the decay $\pi^\pm \rightarrow W^\pm \rightarrow e^\pm \nu_e$. I get $\mathcal{A} = g_w f_\pi q_\mu$, where q_μ is the momentum of the pion. This result can be compared to the standard definition of f_π in terms of the weak axial current matrix element of the pion, $\langle 0 | A_\mu^a | \pi^b \rangle = f_\pi q_\mu \delta^{ab}$. This comparison shows that the coefficient of the kinetic term in the non-linear sigma model is indeed the weak decay constant of the pion.

In the ground state $\Sigma = 1$ and the ground state energy is $E_{vac} = -2B \text{Tr}[M]$. Using the relation $\langle \bar{q}q \rangle = \partial E_{vac} / (\partial m)$ we find $\langle \bar{q}q \rangle = -2B$. Fluctuations around $\Sigma = 1$ determine the masses of the Goldstone bosons. The pion mass satisfies the Gell-Mann-Oaks-Renner relation (GMOR) [17]

$$m_\pi^2 f_\pi^2 = -(m_u + m_d) \langle \bar{q}q \rangle \quad (1.24)$$

and analogous relations exist for the kaon and eta masses. This result shows the characteristic non-analytic dependence of the pion mass on the quark masses, $m_\pi \sim \sqrt{m_q}$.

1.3.2 QCD at finite temperature

The structured of QCD at high temperature can be analyzed using the assumption that quarks and gluons are approximately free. We will see that this assumption is internally consistent, and that it is confirmed by lattice calculations. If the temperature is large then quarks and gluons have thermal momenta $p \sim T \gg \Lambda_{QCD}$. Asymptotic freedom implies that these particles are weakly interacting, and that they form a plasma of mobile color charges, the quark gluon plasma (QGP) [20, 21]. The pressure of a gas of quarks and gluons is

$$P = \frac{\pi^2 T^4}{90} \left(2(N_c^2 - 1) + 4N_c N_f \frac{7}{8} \right). \quad (1.25)$$

This is the Stefan-Boltzmann law, where $2(N_c^2 - 1)$ is the number of bosonic degrees of freedom, and $4N_c N_f$ is the number of fermions. The factor $7/8$ takes into account the difference

between Bose and Fermi statistics. The pressure of a QGP is parametrically much bigger than the pressure of a pion gas, indicating that the QGP at high temperature is thermodynamically stable.

The argument that the QGP at asymptotically high temperature is weakly coupled is somewhat more subtle than it might appear at first glance. If two quarks or gluons in the plasma interact via large angle scattering then the momentum transfer is large, and asymptotic freedom implies that the effective coupling is weak. However, the color Coulomb interaction is dominated by small angle scattering, and it is not immediately clear why the effective interaction that governs small angle scattering is weak. The basic observation is that in a high temperature plasma there is a large thermal population ($n \sim T^3$) of mobile color charges that screen the interaction at distances beyond the Debye length $r_D \sim 1/(gT)$. We also note that even in the limit $T \gg \Lambda_{QCD}$ the QGP contains a non-perturbative sector of static magnetic color fields [22]. This sector of the theory, corresponding to energies below the magnetic screening scale $m_M \lesssim g^2 T$, is strongly coupled, but it does not contribute to thermodynamic or transport properties of the plasma in the limit $T \rightarrow \infty$.

The quark gluon plasma exhibits neither color confinement nor chiral symmetry breaking. This implies that the high temperature phase must be separated from the low temperature hadronic phase by a phase transition. The order of this transition is very sensitive to the values of the quark masses. In QCD with massless u, d and infinitely massive s, c, b, t quarks the transition is second order [23]. In the case of massless (or sufficiently light) u, d, s quarks the transition is first order. Lattice simulations show that for realistic quark masses, $m_u \simeq m_d \simeq 10$ MeV and $m_s \simeq 120$ MeV, the phase transition is a rapid crossover [24, 25]. The transition temperature, defined in terms of the chiral susceptibility, is $T_c \simeq 151 \pm 3 \pm 3$ MeV [26, 27], which is consistent with the result 154 ± 9 MeV reported in [25, 28].

The phase transition is expected to strengthen as a function of chemical potential, so that there is a critical baryon chemical potential μ at which the crossover turns into a first order phase transition [29]. This critical point is the endpoint of the chiral phase transition. Because of the fermion sign problem, which I will discuss in Sect. 1.4.4, it is very difficult to locate the critical endpoint using simulations on the lattice. Model calculations typically predict the existence of a critical point, but do not constrain its location. A number of exploratory lattice calculations have been performed [30–35], but at the time I am writing these notes it has not been demonstrated conclusively that the transition strengthens with increasing baryon chemical potential [36]. The critical endpoint is important because, with the exception of the endpoint of the nuclear liquid-gas transition, it is the only thermodynamically stable point in the QCD phase diagram at which the correlation length diverges. This means that the critical endpoint may manifest itself in heavy ion collisions in terms of enhanced fluctuation observables [37].

1.3.3 High baryon density QCD

The origin of the phase diagram, $T = \mu = 0$, corresponds to the vacuum state of QCD. If we stay on the $T = 0$ line and increase the chemical potential μ then there is no change initially. At zero temperature the chemical potential μ is the energy required to add a baryon to the system, and QCD has a large mass gap for baryonic states. The first non-vacuum state we encounter along the $T = 0$ axis of the phase diagram is nuclear matter, a strongly correlated superfluid composed of approximately non-relativistic neutrons and protons. Nuclear matter is self-bound, and the baryon density changes discontinuously at the onset transition, from $\rho = 0$ to nuclear matter saturation density $\rho = \rho_0 \simeq 0.15 \text{ fm}^{-3}$. The discontinuity decreases as nuclear matter is heated, and the nuclear-liquid gas phase transition ends in a critical point

at $T \simeq 18$ MeV and $\rho \simeq \rho_0/3$ [38–40]. Hot hadronic matter can be described quite accurately as a weakly interacting gas of hadronic resonances. Empirically, the density of states for both mesons and baryons grows exponentially. A system of this type is called a Hagedorn gas, and it is known that a Hagedorn gas has a limiting temperature. It is also known that an exponential density of states can be realized using the string model of hadronic resonances.

In the regime $\mu \gg \Lambda_{QCD}$ we can use arguments similar to those in the limit $T \gg \Lambda_{QCD}$ to establish that quarks and gluons are weakly coupled. At low temperature non-interacting quarks form a Fermi surface, where all states below the Fermi energy $E_F \simeq \mu/3$ are filled, and all states above the Fermi energy are empty. Interactions take place near the Fermi surface, and the corresponding interaction is weak. The main difference between cold quark matter and the hot QGP is that the large density of states near the quark Fermi surface implies that even weak interactions can cause qualitative changes in the ground state of dense matter. In particular, attractive interactions between pairs of quarks ($\mathbf{p}_F, -\mathbf{p}_F$) on opposite sides of the Fermi surface leads to color superconductivity and the formation of a $\langle qq \rangle$ diquark condensate.

Since quarks carry many different quantum numbers, color, flavor, and spin, a variety of superconducting phases are possible. The most symmetric of these, known as the color-flavor locked (CFL) phase, is predicted to exist at asymptotically high density [41, 42]. In the CFL phase the diquark order parameter is

$$\langle q_{\alpha f}^A q_{\beta g}^B \rangle = (C\gamma)_{\alpha\beta} \varepsilon^{ABC} \varepsilon_{fgh} \delta_C^h \Phi, \quad (1.26)$$

where $C\gamma$ is an anti-symmetric (spin zero) Dirac matrix, and Φ determines the magnitude of the gap near the Fermi surface. This order parameter has a number of interesting properties. It breaks the $U(1)$ symmetry associated with baryon number, leading to superfluidity, and it breaks the chiral $SU(3)_L \times SU(3)_R$ symmetry. Except for Goldstone modes the spectrum is fully gapped. Fermions acquire a BCS-pairing gap, and gauge fields are screened by the color Meissner effect. This implies that the CFL phase, even though it is predicted to occur in a very dense liquid of quarks, exhibits many properties of superfluid nuclear matter.

The CFL order parameter describes equal pair-condensates $\langle ud \rangle = \langle us \rangle = \langle ds \rangle$ of all three light quark flavors. As the density is lowered effects of the non-zero strange quark mass become important, and less symmetric phases are predicted to appear [14]. Phases that have been theoretically explored include Bose condensates of pions and kaons, hyperon matter, states with inhomogeneous quark-anti-quark or diquark condensates, and less symmetric color superconducting phases. The regimes of moderate baryon chemical potential in the phase diagram shown in Fig. 1.2 is largely conjecture. Empirical evidence shows that at low μ there is a nuclear matter phase with broken chiral symmetry and zero strangeness, and weak coupling calculations indicate that at high μ we find the CFL phase with broken chiral symmetry but non-zero strangeness. In principle the two phases could be separated by a single onset transition for strangeness [43, 44], but model calculation support a richer picture in which one or more first order transitions intervene, as indicated in Fig. 1.2.

1.4 Lattice QCD

1.4.1 The Wilson action

Symmetry arguments and perturbative calculations can be used to establish general features of the QCD phase diagram, but quantitative results can only be obtained using numerical calculations based on lattice QCD. The same is true for the masses of hadrons, their proper-

ties, and interactions. Lattice QCD is based on the euclidean path integral representation of the partition function, see the contribution by Hatsuda and [45–49] for introductions. More detailed reviews of the lattice field theory approach to hot and dense QCD can be found in [50, 51].

The euclidean partition function for QCD is

$$Z(T, \mu, V) = \int \mathcal{D}A_\mu \mathcal{D}q_f \mathcal{D}\bar{q}_f \exp(-S_E), \quad (1.27)$$

where S_E is the euclidean action

$$S_E = - \int_0^\beta d\tau \int_V d^3x \mathcal{L}^E, \quad (1.28)$$

$\beta = T^{-1}$ is the inverse temperature and \mathcal{L}^E is the euclidean Lagrangian, which is obtained by analytically continuing equ. (1.16) to imaginary time $\tau = it$. As in the quantum mechanical example in equ. (1.4) the temperature enters via the boundary condition on the fields in the imaginary time direction. Gauge fields and fermions obey periodic and anti-periodic boundary conditions, respectively. The chemical potential enters through its coupling to the conserved baryon density

$$\mathcal{L}^E(\mu) = \mathcal{L}^E(0) + \mu \bar{q}_f \gamma_0 q_f. \quad (1.29)$$

In his pioneering work Wilson proposed to discretize the action on a $N_\tau \times N_\sigma^3$ space-time lattice with lattice spacings a_τ and a_σ [52]. In many cases $a_\sigma = a_\tau = a$, but we will encounter an exception in Sect. 1.5.4. when we discuss the Hamiltonian formulation of the theory.

At finite temperature we have to ensure that the spatial volume is larger than the inverse temperature, $L > \beta$. Here, $\beta = N_\tau a_\tau$, $L = N_\sigma a_\sigma$, and $V = L^3$ is the volume. Thermodynamic quantities are determined by taking derivatives of the partition function. The energy and baryon density are given by

$$\mathcal{E} = - \frac{1}{V} \left. \frac{\partial \log Z}{\partial \beta} \right|_{\beta, \mu}, \quad (1.30)$$

$$\rho = \frac{1}{\beta V} \left. \frac{\partial \log Z}{\partial \mu} \right|_{\beta}. \quad (1.31)$$

The discretized action for the gauge fields originally suggested by Wilson is given by

$$S_W = - \frac{2}{g^2} \sum_n \sum_{\mu < \nu} \text{Re Tr} [W_{\mu\nu}(n) - 1] \quad (1.32)$$

where $W_{\mu\nu}(n)$ is the plaquette, the product of gauge links around an elementary loop on the lattice,

$$W_{\mu\nu}(n) = U_\mu(n) U_\nu(n + \hat{\mu}) U_{-\mu}(n + \hat{\mu} + \hat{\nu}) U_{-\nu}(n + \hat{\nu}). \quad (1.33)$$

Here, $n = (n_\tau, n_i)$ labels lattice sites and $\hat{\mu}$ is a unit vector in the μ -direction. The gauge links $U_\mu(n)$ are $SU(N_c)$ matrices. We can think of the gauge links as line integrals

$$U_\mu(n) = \exp(iaA_\mu(n)), \quad (1.34)$$

and of the plaquettes as fluxes

$$W_{\mu\nu}(n) = \exp(ia^2 G_{\mu\nu}(n)), \quad (1.35)$$

but the fundamental variables in the path integral are the (compact) group variables U_μ , not the (non-compact) gauge potentials A_μ . In particular, the path integral in pure gauge QCD

takes the form

$$Z = \int \prod_{n,\mu} dU_\mu(n) \exp(-S_W), \quad (1.36)$$

where dU is the Haar measure on $SU(N_c)$. The Haar measure describes the correct integration measure for the gauge group. Some group integrals are discussed by Hatsuda, but part of the beauty of the Metropolis method is that we never have to explicitly construct $dU_\mu(n)$.

Using equ. (1.34) we can check that the Wilson action reduces to continuum pure gauge theory in the limit $a \rightarrow 0$. We note that the gauge invariance of QCD is maintained exactly, even on a finite lattice, but that Lorentz invariance is only restored in the continuum limit. We also observe that classical scale invariance implies that the massless QCD action is independent of a . The continuum limit is taken by adjusting the bare coupling at the scale of the lattice spacing according to asymptotic freedom, see equ. (1.19). In practice the lattice spacing is not small enough to ensure the accuracy of this method, and more sophisticated scale setting procedures are used [50, 51].

Monte Carlo simulations of the path integral equ. (1.36) can be performed using the Metropolis algorithm explained in Sect. 1.2:

- Initialize the link variables with random $SU(N_c)$ matrices. A simple algorithm is based on writing U in terms of N_c complex row vectors \mathbf{u}_i . Take each vector to be random unit vector and then use the Gram-Schmidt method to orthogonalize the different vectors, $\mathbf{u}_i \cdot \mathbf{u}_j^* = \delta_{ij}$. This ensures that U is unitary and distributed according to the $SU(N_c)$ Haar measure [53].
- Sweep through the lattice and update individual link variables. For this purpose multiply the link variable by a random $SU(N_c)$ matrix, $U_\mu \rightarrow RU_\mu$. Compute the change in the Wilson action and accept the update with probability $\exp(-\Delta S_W)$.
- Compute physical observables. The simplest observable is the average plaquette $\langle W_{\mu\nu} \rangle$, which can be related to the equation of state, see equ. (1.30). More complicated observables include the correlation function between plaquettes, and the Wilson loop

$$W(\mathcal{C}) = \text{Tr}[L(\mathcal{C})], \quad L(\mathcal{C}) = \prod_{(n,\mu) \in \mathcal{C}} U_\mu(n), \quad (1.37)$$

where $L(\mathcal{C})$ is the product of link variables around a closed loop. The average Wilson loop is related to the potential between two static charges in the fundamental representation

$$V(R) = - \lim_{T \rightarrow \infty} \frac{1}{T} \log[\langle W(\mathcal{C}) \rangle], \quad (1.38)$$

where $R \times T$ is the area of a rectangular loop \mathcal{C} .

- Tune to the continuum limit $a \rightarrow 0$ by adjusting the coupling constant according to the asymptotic freedom formula equ. (1.19). Note that the Lambda parameter for the lattice regulator is quite small, $\Lambda_{lat} = \Lambda_{MS}/28.8$ [54]. Also observe that we have to increase N_σ, N_τ to keep the physical volume constant as $a \rightarrow 0$. Indeed, once the continuum limit $a \rightarrow 0$ is reached we have to study the infinite volume (thermodynamic) limit $V \rightarrow \infty$. This is more difficult than it appears, because $a \rightarrow 0$, corresponding to $g \rightarrow 0$, is a critical point of the partition function (1.36), and simulations exhibit critical slowing down.

Metropolis simulations with the pure gauge Wilson action are very simple and robust. As an illustration I provide a simple Z_2 lattice gauge theory code written by M. Creutz in the appendix. Reasonable results for the heavy quark potential can be obtained on fairly coarse lattices, for example an 8^4 lattice with a spacing $a \simeq 0.25$ fm [55]. However, accurate results with controlled error bars require significant computational resources. In practice the perturbative relation between a and g^2 is only valid on very fine lattices, and the scale setting has to be done non-perturbatively. Also, determining the spectrum of pure gauge theory is

difficult. Purely gluonic states, glueballs, are quite heavy, with masses in the range $m \simeq 1.6$ GeV and higher. This implies that gluonic correlation functions are short range, requiring a resolution $a \simeq 0.1$ fm or better. Finally, simulations on fine lattices are affected by critical slowing down. Indeed, finding an efficient method for updating gauge fields on very fine lattices, analogous to the cluster algorithms for spin models [56], is an important unsolved problem.

1.4.2 Fermions on the lattice

The main difficulty in lattice QCD is related to the presence of light fermions. The fermion action is of the form

$$S_F = a^4 \sum_{m,n} \bar{q}(m) D_{mn} q(n). \quad (1.39)$$

Formally, the integration over the fermion fields can be performed exactly, resulting in the determinant of the Dirac operator $\det(D(A_\mu, \mu))$. Several methods exist for discretizing the Dirac operator D , and for sampling the determinant. Different discretization schemes differ in the degree to which chiral symmetry is maintained on a finite lattice. The original formulation due to Wilson [52] preserves no chiral symmetry, the staggered Fermion scheme [57] maintains a subset of the full chiral symmetry, while the domain wall [58] and overlap methods [59] aim to preserve the full chiral symmetry on a discrete lattice.

The central difficulty in implementing these methods is that the fermion determinant is a very non-local object. While updating a single gauge link only requires recalculating a small number of plaquettes (6 in $d = 4$ dimensions) in the Wilson action, recalculating the fermion action requires computing the determinant of a (very sparse) matrix of size $(N_\tau N_\sigma^3) \times (N_\tau N_\sigma^3)$ or larger. This is clearly impractical. Fermion algorithms rely on a number of tricks. The first is the observation that the Dirac operator has a property called γ_5 -hermiticity, $\gamma_5 D \gamma_5 = D^\dagger$, which implies that $\det(D)$ is real. The determinant of a two-flavor theory is then real and positive. This allows us to rewrite the fermion determinant as a path integral over a bosonic field with a non-local but positive action

$$\det(D_u) \det(D_d) = \det(DD^\dagger) = \int \mathcal{D}\phi \mathcal{D}\phi^\dagger \exp(-\phi^\dagger (DD^\dagger)^{-1} \phi). \quad (1.40)$$

The path integral over the pseudofermion field ϕ can be sampled using a combination of deterministic methods like molecular dynamics and stochastic methods such as the Metropolis algorithm. These combined algorithms are known as Hybrid Monte Carlo (HMC) methods. Codes that implement the HMC algorithm for pseudofermions are significantly more complicated than the Metropolis algorithm for the pure gauge Wilson action discussed above, and I refer the interested reader to the more specialized literature [60]. I also note that since these algorithms involve the calculation of D^{-1} the computational cost increases as the quark masses are lowered.

The calculation of correlation functions also differs from the bosonic case. Consider, for example, an operator with the quantum numbers of a charged pion, $J_\pi(x) = \bar{u}^a(x) \gamma_5 d^a(x)$. Since the fermion action is quadratic the correlation function in a given gauge configuration can be computed exactly in terms of the fermion propagator. The full correlation function is

$$\Pi_\pi(x) = \langle J_\pi(x) J_\pi(0) \rangle = \langle \text{Tr} [S(x,0) \gamma_5 S(0,x) \gamma_5] \rangle, \quad (1.41)$$

where $S(x,y) = \langle x | D^{-1} | y \rangle$ is the fermion propagator, and we have assumed exact isospin symmetry so that the propagator of the up quark is equal to the propagator of the down quark. Note that the interaction between quarks is encoded in the average over all gauge fields. The

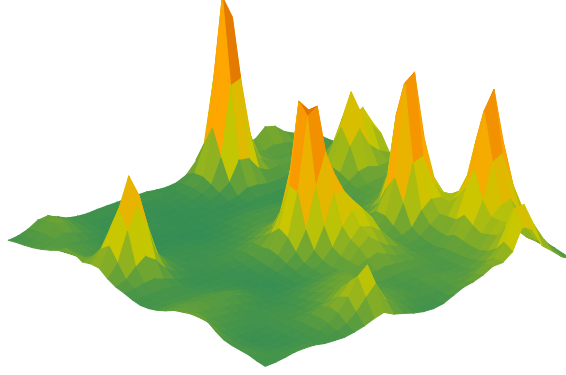


Fig. 1.3 Topological objects in lattice QCD (figure courtesy of S. Sharma, see [62]). This picture shows a slice through a low lying eigenstate of the Dirac operator in lattice QCD.

one-gluon exchange interaction, for example, corresponds to a perturbative fluctuation in the gauge field that modifies the two quark propagators. An operator with the quantum number of the proton is $\eta_\alpha(x) = \epsilon_{abc}(u^a(x)C\gamma_\mu u^b(x))(\gamma^\mu\gamma_5 d^c(x))_\alpha$. The correlation function is

$$\Pi_{\alpha\beta}(x) = 2\epsilon_{abc}\epsilon_{a'b'c'} \left\langle \left(\gamma_\mu\gamma_5 S^{cc'}(0,x)\gamma_\nu\gamma_5 \right)_{\alpha\beta} \text{Tr} \left[\gamma_\mu S^{aa'}(0,x)\gamma_\nu C(S^{bb'}(0,x))^T C \right] \right\rangle. \quad (1.42)$$

Note that meson correlation function involves one forward and one backward going propagator, whereas the propagators in the baryon correlation function are all forward going. A difficulty arises when we consider flavor singlet $\bar{q}q$ currents such as $J_{\eta'} = (\bar{u}^a(x)\gamma_5 u^a(x) + \bar{d}^a(x)\gamma_5 d^a(x))/\sqrt{2}$, which has the quantum numbers of the η' meson. We find

$$\Pi_{\eta'}(x) = \langle J_{\eta'}(x)J_{\eta'}(0) \rangle = \langle \text{Tr}[S(x,0)\gamma_5 S(0,x)\gamma_5] - 2\text{Tr}[S(x,x)\gamma_5] \text{Tr}[S(0,0)\gamma_5] \rangle, \quad (1.43)$$

which involve propagators $S(x,x)$ that loop back to the same point. These contributions are known as quark-line disconnected diagrams, and difficult to treat numerically, see [61] for a recent discussion.

1.4.3 The QCD vacuum

It is natural to hope that lattice QCD can provide us with an intuitive picture of what the QCD vacuum looks like, similar to the picture of the quantum mechanical ground state shown in Fig. 1.1. This turns out to be more complicated, for a number of reasons. The first is that the field in QCD is a $SU(3)$ matrix, which is hard to visualize. The second, more important, problem is related to quantum fluctuations. In QCD there is no obvious separation of scales that would allow us to clearly separate perturbative fluctuations from large semi-classical fluctuations.

This has led to the idea to eliminate short range fluctuations by some kind of filtering or smoothing algorithm. The simplest of these is known as cooling [63]. In the cooling method

we modify the Metropolis algorithm so that only updates that reduce the action are accepted. Since the update algorithm is local, this will tend to eliminate small structures but preserve larger objects. A modern version of cooling is gradient flow [64]. In the gradient flow method we continue the gauge fields to a 5th “time” dimension. In this direction the fields satisfy a differential equation

$$\partial_\tau A_\mu = D^\nu G_{\mu\nu}, \quad (1.44)$$

where $A_\mu(\tau = 0)$ is the four-dimensional gauge field and the rhs is computed from the gauge potentials evaluated at the flow time τ . The Lorentz indices remain four-dimensional. The rhs of the flow equations is the classical equation of motion, so that the gradient flow tends to drive gauge fields towards the closest classical solution. The only finite action solutions of the euclidean field equations on R^4 are instantons [65, 66]. Instantons and anti-instantons are characterized by integer values $Q_{top} = \pm 1$ of the topological charge

$$Q_{top} = \int d^4x q(x), \quad q(x) = \frac{g^2}{64\pi^2} \epsilon^{\mu\nu\alpha\beta} G_{\mu\nu}^a G_{\alpha\beta}^a. \quad (1.45)$$

Exact higher charge solutions exist, but the QCD vacuum is dominated by configurations with both instantons and anti-instantons. These gauge field configurations are only approximate solutions of the equations of motion [66]. Under cooling or gradient flow instantons and anti-instantons will eventually annihilate and evolve to an exact multi-instantons solution with $Q_{top} = N_I - N_A$, where $N_{I,A}$ are the numbers of (anti)instantons. However, the $N_I + N_A$ topological objects are preserved for flow times that are much longer than the decay time of ordinary quantum fluctuations, and the total number of well separated instantons and anti-instantons can be determined.

The average topological charge is zero, but the pure gauge vacuum is characterized by a non-zero topological susceptibility

$$\chi_{top} = \frac{1}{V} \langle Q_{top}^2 \rangle, \quad (1.46)$$

where V is the euclidean four-volume. The topological charge can be determined using the naive lattice discretization of equ. (1.45), but this operator is very noisy, and in general not an integer. This problem can be addressed using the cooling or gradient flow algorithms discussed above. Recent lattice calculations based on these methods give $\chi_{top} = (190 \pm 5 \text{ MeV})^4$ [67, 68]. A simple picture of the QCD vacuum which is consistent with this value is the dilute instanton liquid model, which assumes that the topological susceptibility is determined by Poisson fluctuations in an ensemble of instantons and anti-instantons with an average density $(N_I + N_A)/V \simeq 1 \text{ fm}^{-4}$ [66]. This is an approximate picture, and more complicated configurations involving monopoles and fractional charges are needed to understand the large N_c limit and the role of confinement [69].

Another important development is the use of fermionic methods to analyze the vacuum structure of QCD. In a given gauge configuration the quark propagator can be written as

$$S(x, y) = \sum_\lambda \frac{\psi_\lambda(x) \psi_\lambda^\dagger(y)}{\lambda + im}, \quad (1.47)$$

where ψ_λ is an eigenvector of the Dirac operator with eigenvalue λ : $D\psi_\lambda = (\lambda + im)\psi_\lambda$. Note that this is not how propagators are typically determined in lattice QCD, because the calculation of the complete spectrum is numerically very expensive. Gamma five hermiticity implies that eigenvalues come in pairs $\pm\lambda$. The quark condensate is given by

$$\langle \bar{q}q \rangle = -i \int d^4x \langle \text{Tr} [S(x, x)] \rangle = - \left\langle \sum_{\lambda > 0} \frac{2m}{\lambda^2 + m^2} \right\rangle. \quad (1.48)$$

Here, I have ignored the contribution from exact zero modes because the density of zero modes is suppressed by m^{N_f} . This factor comes from the determinant in the measure. If we were to ignore the determinant (this is called the quenched approximation), then the quark condensate would diverge as $1/m$. We observe that a finite value of the quark condensate in the chiral limit $m \rightarrow 0$ requires an accumulation of eigenvalues near zero. This can be made more explicit by introducing the density of states

$$\rho(v) = \left\langle \sum_{\lambda \geq 0} \delta(\lambda - v) \right\rangle. \quad (1.49)$$

The chiral condensate in the thermodynamic and chiral limits is given by

$$\langle \bar{q}q \rangle = -\pi\rho(0). \quad (1.50)$$

This is known as the Banks-Casher relation [70]. Note that it is essential to take the thermodynamic $V \rightarrow \infty$ limit before the chiral limit $m \rightarrow 0$.

Exact zero modes of the Dirac operator are related to topology. The Dirac operator has one left handed zero mode in the field of an instanton, and a right handed zero mode in the field of an anti-instanton. This is consistent with the Atiyah-Singer index theorem, which states that the topological charge is equal to the index of the Dirac operator, the difference between the number of left and right handed zero modes, $Q_{top} = N_f(n_L - n_R)$. These results suggest that it is possible to give a purely fermionic definition of the topological charge density.

On the lattice, this can be achieved for a class of Dirac operators that satisfy the Ginsparg-Wilson relation [71]

$$D\gamma_5 + \gamma_5 D = aD\gamma_5 D, \quad (1.51)$$

where a is the lattice spacing. In the continuum limit we recover the expected relation $D\gamma_5 + \gamma_5 D = 0$ for the massless Dirac operator. The important observation is that the fermionic topological density

$$q_f(n) = \frac{1}{2a^3} \text{tr}_{CD} [\gamma_5 D(n, n)], \quad (1.52)$$

where tr_{CD} is a color-Dirac trace, satisfies the index theorem

$$Q_{top} = a^4 \sum_n q_f(n) \quad (1.53)$$

on a discrete lattice. Fig. 1.3 shows the absolute square of $q_f(x)$ constructed from lying eigenmodes of the Dirac operator. We observe that fermionic operators can indeed be used to probe the topological content of the QCD vacuum directly, without the need for filtering or smoothing.

The existence of zero mode implies that the topological susceptibility is zero if at least one quark flavor is massless. This is because the path integral measure contains the fermion determinant, which vanishes if $m = 0$ and $Q_{top} \neq 0$. We can be more precise using the chiral lagrangian eq. (1.22). In order to keep track of topology we add to the QCD action a topological term $S_\theta = i\theta Q_{top}$. Then the topological susceptibility is given by the second derivative of the free energy with respect to θ . Since every zero mode in the Dirac operator contributes a factor $\det(M)$ to the partition function we know that θ enters the effective lagrangian in the combination $\theta + \arg(\det(M))$. The vacuum energy is determined by

$$V = -B\text{Tr} \left[M e^{i\theta/N_f} \Sigma^\dagger \right] + h.c., \quad (1.54)$$

and we observe that the topological susceptibility in QCD with degenerate quark masses is proportional to $m\langle \bar{q}q \rangle$. Note that eq. (1.54) is consistent with the vanishing of χ_{top} for $m_u = 0$.

If $m_u = 0$ and $m_d \neq 0$ then equ. (1.54) is minimized by $\Sigma = \exp(i\phi\tau_3)$ with $\phi = \theta/2$, and the vacuum energy is independent of θ .

It is tempting to think that exact zero modes, governed by topology, and approximate zero modes, connected to chiral symmetry breaking, are related. This is the basis of the instanton liquid model [66]. In the instanton liquid model we consider an ensemble of instantons and anti-instantons with no (or small) net topology. The exact zero modes of individual instantons are lifted, and form a zero mode zone. The density of eigenvalues in the zero mode zone determines the chiral condensate via the Banks-Casher relation. This model predicts the correct order of magnitude of $\langle \bar{q}q \rangle$, but the calculation cannot be systematically improved because chiral symmetry breaking requires strong coupling. Recently, we showed that the connection of chiral symmetry breaking, instantons and monopoles can be made precise in a certain limit of QCD. The idea is to compactify QCD on $R^3 \times S_1$, where the size of the circle is much smaller than Λ_{QCD}^{-1} , and the fermions satisfy non-thermal (twisted) boundary conditions [72].

1.4.4 Lattice QCD at finite baryon density

In section 1.4.2 I discussed some of the difficulties that appear when we discretize the Dirac operator. A separate, more serious, issue with fermions is that for $\mu \neq 0$ the Dirac operator does not satisfy γ_5 -hermiticity. This implies that the fermion determinant is no longer real, and that standard importance sampling methods fail. This is the “sign” problem already mentioned in Sect. 1.3.2. To understand the severity of the problem consider a generic expectation value

$$\langle \mathcal{O} \rangle = \frac{\int dU \det(D) \mathcal{O} e^{-S}}{\int dU \det(D) e^{-S}}. \quad (1.55)$$

If the determinant is complex I can write this as

$$\langle \mathcal{O} \rangle = \frac{\int dU |\det(D)| \mathcal{O} e^{i\varphi} e^{-S}}{\int dU |\det(D)| e^{i\varphi} e^{-S}} \equiv \frac{\langle \mathcal{O} e^{i\varphi} \rangle_{pq}}{\langle e^{i\varphi} \rangle_{pq}}, \quad (1.56)$$

where $\langle \cdot \rangle_{pq}$ refers to a phase quenched average. This average can be computed using the Metropolis (or HMC) algorithm. The problem is that the average phase $\langle e^{i\varphi} \rangle_{pq}$ is very small. This follows from the fact that the average phase can be expressed as the ratio of two partition functions

$$\langle e^{i\varphi} \rangle_{pq} = \frac{\int dU \det(D) e^{-S}}{\int dU |\det(D)| e^{-S}} = \frac{Z}{Z_{pq}} = e^{-V\Delta F}, \quad (1.57)$$

where ΔF is the free energy density difference, and V is the volume of the system. This shows that the phase is exponentially small, and that the ratio equ. (1.56) is very difficult to compute.

As a specific example consider QCD with two degenerate flavors, up and down, and a baryon chemical potential $\mu_u = \mu_d = \mu_B/3$. Then $\det(D) = \det(D_u)\det(D_d)$ and $|\det(D)| = \det(D_u)\det(D_d)^*$. The phase quenched partition function Z_{pq} can be interpreted as the partition function of QCD with a non-zero isospin chemical potential $\mu_u = -\mu_d = \mu_I/2$. The small μ behavior of both the isospin and baryon number theories at $T = 0$ is easily understood. The isospin theory has a second order phase transition at $\mu_I = m_\pi$ which corresponds to the onset of pion condensation. The baryon theory has a first order transition at $\mu_B = m_p - B$, where $B \simeq 15$ MeV is the binding energy of infinite nuclear matter. This implies that for $\mu > m_\pi$ the partition functions Z and Z_{pq} describe very different physical systems, and the sign problem is severe.

The sign problem may manifest itself in different ways. Consider, for example, an attempt to study the correlation function of A nucleons in a QCD ensemble generated at $\mu_B = 0$. For

large A this correlation function determines the binding energy of nuclear matter. There are two difficulties with this approach. The first is that the operator contains $3A$ quark fields, so that the correlator has up to $(3A)!$ contractions. This is not prohibitive, because the number of contractions can be reduced using symmetries and iterative algorithms. Indeed, correlators for medium mass nuclei have been computed [49]. The second, more serious, problem is the signal-to-noise ratio. The variance of the correlator C is

$$\text{var}(C) = \langle CC^\dagger \rangle - \langle C \rangle^2. \quad (1.58)$$

The A nucleon correlator C contains $3A$ forward going quark propagators, and CC^\dagger consists of $3A$ forward and $3A$ backward propagators. This implies that CC^\dagger couples to a state of $3A$ mesons. Since the lightest meson is the pion and the lightest baryon is the proton the signal-to-noise of an A nucleon correlation function is

$$\frac{\mathcal{S}}{\mathcal{N}} \sim \exp(-A(m_p - 3m_\pi/2)\tau). \quad (1.59)$$

In order to resolve the ground state with a given A we have to make τ sufficiently large so that excited states with the same A are suppressed. For $A = 1$ there is a πN continuum starting an excitation energy $\Delta E = m_\pi$, and the first resonance at $\Delta E = m_\Delta - m_N \simeq 300$ MeV. This means that we have to consider $\tau \gtrsim 1$ fm. For multi-nucleon states the situation is more complicated, because there are many closely spaced multi-nucleon states in a finite volume. The problem is studied, for example, in [73]. The conclusion is that different bound and scattering states are separated by 10s of MeV, requiring $\tau \gtrsim 4$ fm. It may be possible to improve on this estimate by using variationally improved sources, but even for $\tau \simeq 2$ fm the signal to noise is extremely poor for $A \gtrsim 4$. This shows that in simulations with fixed A the sign problem manifests itself as a noise problem. This is not surprising. One way to think about the sign problem is to view it as an overlap problem. The configurations that contribute to Z_{pq} have poor overlap with those that contribute to Z . The same phenomenon is at work here. Configurations generated at $\mu_B = 0$ reflect vacuum physics, and the lightest fermionic fluctuation is a pion. Large cancellations are required to explore the physics of multi-baryon states.

There are many attempts to find direct solutions to the sign problem, but at this time the only regime in which controlled calculations are feasible is the regime of small μ and high T . In this region the partition function can be expanded in a Taylor series in μ/T . The corresponding expansion coefficients are generalized susceptibilities that can be determined from lattice simulations at zero chemical potential. The susceptibilities not only determine the equation of state at finite baryon density, but also control fluctuations of conserved charges.

In addition to methods that are restricted to the regime $\mu \lesssim \pi T$, a number of proposals to explore QCD at high baryon density are being pursued. This includes new approaches, like integration over Lefschetz thimbles [74, 75], as well as novel variants of old approaches, like the complex Langevin method [76, 77], or the use of dual variables [78]. The ultimate promise of these methods is still unclear, but the central importance of the sign problem to computational physics continues to attract new ideas.

1.4.5 Real time properties

The basic trick in lattice QCD is the continuation of the path integral to imaginary time. This makes it possible to calculate the path integral by importance sampling, but it implies that we only have direct access to imaginary time correlation functions. For many observables this is not a serious problem. Thermodynamic observables, for example, are static quantities and no analytic continuation is necessary. The ground state contribution to a hadron correlation

function is $\Pi(\tau) \sim e^{-m_H \tau}$ which is trivially continued to $\Pi(t) \sim e^{-im_H t}$. However, difficulties arise if one studies excited states, in particular resonances, the interaction between hadrons, or the real time response of many body systems at finite temperature and density.

Significant progress has been made in studying scattering processes, at least in the elastic regime. This is discussed in some of the later chapters of this book. Here, I will concentrate on the calculation of real time response functions. The prototypical example is the calculation of the shear viscosity of a QCD plasma using the retarded correlation function of the stress tensor T^{xy} ,

$$G_R^{xy,xy}(\omega, \mathbf{k}) = -i \int dt \int d^3x e^{i(\omega t - \mathbf{k} \cdot \mathbf{x})} \Theta(t) \langle [T^{xy}(\mathbf{x}, t), T^{xy}(0, 0)] \rangle, \quad (1.60)$$

The associated spectral function is defined by $\rho(\omega, \mathbf{k}) = -\text{Im} G_R(\omega, \mathbf{k})$. The imaginary part of the retarded correlator is a measure of dissipation. This relation can be made more precise using fluid dynamics, which is an effective theory of the response function in the low energy, small momentum limit [79, 80].

Linearized fluid dynamics shows that the static response function is determined by the pressure of the fluid, and that the leading energy and momentum dependence is governed by transport coefficients. These relations can be used to derive Kubo formulas, expressions for the transport coefficients in terms of retarded correlation functions. The Kubo relation for the shear viscosity is

$$\eta = \lim_{\omega \rightarrow 0} \lim_{k \rightarrow 0} \frac{\rho^{xy,xy}(\omega, \mathbf{k})}{\omega}, \quad (1.61)$$

and similar results hold for the bulk viscosity, the thermal conductivity, and heavy quark diffusion constants.

The spectral function contains information about the physical excitations that carry the response. The euclidean path integral does not provide direct access to the retarded correlator or the spectral function. Lattice calculations are based on the relation between the spectral function and the imaginary energy (Matsubara) correlation function

$$G_E(i\omega_n) = \int \frac{d\omega}{2\pi} \frac{\rho(\omega)}{\omega - i\omega_n}, \quad (1.62)$$

where $\omega_n = 2\pi nT$ is the Matsubara frequency. The imaginary time correlation function is

$$G_E(\tau) = \int \frac{d\omega}{2\pi} K(\omega, \tau) \rho(\omega), \quad (1.63)$$

where the kernel $K(\omega, \tau)$ is given by

$$K(\omega, \tau) = \frac{\cosh[\omega(\tau - 1/(2T))]}{\sinh[\omega/(2T)]} = [1 + n_B(\omega)] e^{-\omega\tau} + n_B(\omega) e^{\omega\tau}, \quad (1.64)$$

and $n_B(\omega)$ is the Bose distribution function. The imaginary time correlation function equ. (1.63) was studied on the lattice in [81–84]. The basic idea for calculating transport coefficients is to numerically compute $G_E(\tau)$, invert the integral transform in equ. (1.63) to obtain the spectral functions $\rho(\omega)$, and then study the limit $\omega \rightarrow 0$.

The problem is that $G_E(\tau)$ is computed on a small number of discrete lattice sites, and that the imaginary time correlator at distances on the order of $\beta/2$ is not very sensitive to the slope of the spectral function at low energy. Recent attempts to address these problems and to obtain numerically stable spectral functions and reliable error estimates are based on Bayesian methods such as the maximum entropy method mentioned in Sect. 1.2, see [85, 86]. It is also possible to optimize the contribution from the transport peak by measuring the correlation functions of conserved charges, such as energy and momentum density, at non-zero spatial momentum [87, 88]. A possible issue with lattice calculations is that effects of

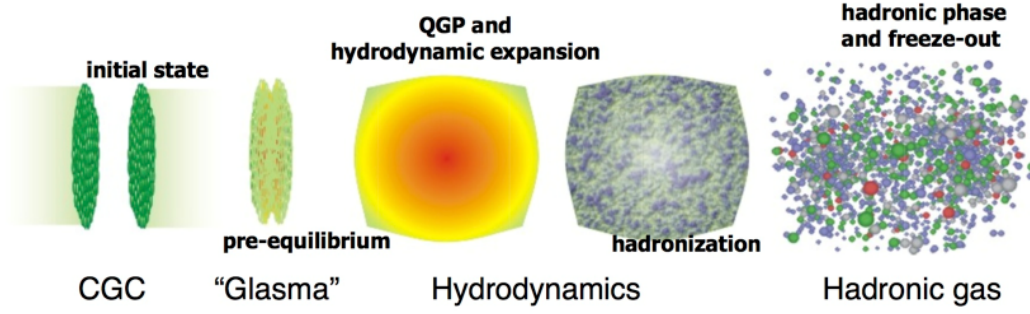


Fig. 1.4 Schematic time evolution of a heavy ion collision. Figure courtesy of S. Bass. CGC refers to the color glass condensate, a semi-classical model of the overpopulated gluon configuration in the initial state of a heavy ion collision. Glasma refers to the non-equilibrium evolution of this state into a locally equilibrated plasma. Hydrodynamics is the theory of the time evolution of a locally equilibrated fireball, and hadronic phase refers to the late time kinetic stage of the collision.

poor resolution tend to bias the result towards small values of η/s , where s is the entropy density. The finite temperature spectral function satisfies the sum rule [89]

$$\frac{2}{\pi} \int d\omega [\eta(\omega) - \eta_{T=0}(\omega)] = \frac{3}{10} sT, \quad (1.65)$$

where $\eta(\omega) = \rho(\omega)/\omega$. On the lattice it is difficult to resolve sharp features in the spectral function. Roughly, the resolution is limited by the lowest Matsubara frequency πT . I will therefore assume that the $T \neq 0$ spectral function is a Lorentzian with width πT

$$\eta(\omega) - \eta_{T=0}(\omega) \simeq \frac{\eta(0)(\pi T)^2}{\omega^2 + (\pi T)^2}. \quad (1.66)$$

Then the integral on the lhs is equal to $\eta(0)\pi T$, and the sum rule predicts $\eta/s \sim 3/(10\pi)$, quite close to $\eta/s = 1/(4\pi)$. The lesson is that it is easy to obtain small values of η/s , and much more difficult to obtain large values of η/s , predicted by perturbative QCD [90].

The first calculation of the shear viscosity on the lattice was performed by Karsch and Wyld [81]. More recently, the problem of computing the shear and bulk viscosity in a pure gauge plasma near T_c was revisited by Meyer [82, 88]. He obtains $\eta/s = 0.102(56)$ and $\zeta/s = 0.065(17)$ at $T = 1.24T_c$. Shear viscosity is only weakly dependent on temperature, but bulk viscosity is strongly peaked near T_c . The value of η/s is consistent with experimental results, and with the prediction from holographic duality, $\eta/s = 1/(4\pi)$ [91].

1.5 Nonequilibrium QCD

In the remainder of this chapter I will discuss a number of coarse grained approaches to the non-equilibrium dynamics of QCD. These methods are relevant to the study of nuclear collisions, in particular in the ultra-relativistic regime. This regime is explored experimentally at the Relativistic Heavy Ion Collider (RHIC) at Brookhaven National Laboratory and the Large Hadron Collider (LHC) at CERN. A rough time line of a heavy ion collision is shown in Fig. 1.4. Initial nucleon-nucleon collisions release a large number of quarks and gluons. This process is described by the full non-equilibrium quantum field theory, but there are a number of approximate descriptions that may be useful in certain regimes. The first is a classical field

theory description in terms of highly occupied classical gluon fields. The second is a kinetic theory in terms of quark and gluon quasi-particles. Finally, there is a new approach, which is a description in terms of a dual gravitational theory.

Theories of the initial state demonstrate that there is a tendency towards local equilibration. If local equilibrium is achieved then a simpler theory, fluid dynamics is applicable. Fluid dynamics is very efficient in the sense that it deals with a small number of variables, the conserved densities of particle number, energy and momentum, and that it has very few parameters, an equation of state and a set of transport coefficients. The fluid dynamic stage of a heavy ion collision has a finite duration. Eventually the density becomes too low and local equilibrium can no longer be maintained. At this point kinetic theory is again relevant, now formulated in terms of hadronic quasi-particles. All the theories we have mentioned, fluid dynamics, kinetic theory, classical field theory, and holography, have reached a high degree of sophistication and I will point to text books and review for detailed introductions. Nevertheless, the basic ideas are quite simple, and I will provide some examples in the following sections.

1.5.1 Fluid Dynamics

I begin with fluid dynamics, because it is the most general and in some ways the simplest non-equilibrium theory. It is important to remember, however, that fluid dynamics is a very rich framework, both mathematically and in terms of the range of phenomena that one may encounter. In the following I will focus on the non-relativistic theory. There is no fundamental difference between the relativistic and non-relativistic theories, but some simplifications appear in the non-relativistic regime. Non-relativistic fluid dynamics is used in many areas of physics, including the physics of cold atomic Fermi gases and neutron stars. The relativistic theory is relevant to high energy heavy ion collisions and supernova explosions. Introductions to relativistic fluid dynamics can be found in [92–94].

Fluid dynamics reduces the complicated non-equilibrium many-body problem to equations of motion for the conserved charges. The reason that this is possible is the separation of scales between the microscopic collision time τ_{micro} , and the relaxation time τ_{macro} of hydrodynamic variables. A generic perturbation of the system decays on a time scale on the order of τ_{micro} , irrespective of the typical length scale involved. Here, τ_{micro} is determined by microscopic time scales, such as the typical collision time between quasi-particles. A fluctuation of a conserved charge, on the other hand, cannot decay locally and has to relax by diffusion or propagation. The relevant time scale τ_{macro} increases with the length scale of the perturbation. As a consequence, when we focus on sufficiently large scales we can assume $\tau_{macro} \gg \tau_{micro}$, and focus on the evolution of conserved charges.

In a simple non-relativistic fluid the conserved charges are the mass density ρ , the momentum density π , and the energy density \mathcal{E} . The momentum density can be used to define the fluid velocity, $\mathbf{u} = \pi/\rho$. By Galilean invariance the energy density can then be written as the sum of the internal energy density and the kinetic energy density, $\mathcal{E} = \mathcal{E}_0 + \frac{1}{2}\rho u^2$. The conservation laws are

$$\frac{\partial \rho}{\partial t} = -\nabla \cdot \pi, \quad (1.67)$$

$$\frac{\partial \pi_i}{\partial t} = -\nabla_j \Pi_{ij}, \quad (1.68)$$

$$\frac{\partial \mathcal{E}}{\partial t} = -\nabla \cdot \mathbf{j}^\mathcal{E}. \quad (1.69)$$

In order for these equations to close we have to specify constitutive relations for the stress tensor Π_{ij} and the energy current \mathbf{j}^ε . Since fluid dynamics is an effective long wavelength theory we expect that the currents can be systematically expanded in gradients of the hydrodynamic variables ρ , \mathbf{u} and \mathcal{E}_0 . At leading order the stress tensor contains no derivatives and the structure is completely fixed by rotational symmetry and Galilean invariance. We have

$$\Pi_{ij} = \rho u_i u_j + P \delta_{ij} + \delta \Pi_{ij}, \quad (1.70)$$

where $P = P(\rho, \mathcal{E}_0)$ is the equation of state and $\delta \Pi_{ij}$ contains gradient terms. The approximation $\delta \Pi_{ij} = 0$ is called ideal fluid dynamics, and the equation of motion for π is known as the Euler equation. Ideal fluid dynamics is time reversal invariant and the entropy is conserved. If gradient terms are included then time reversal invariance is broken and the entropy increases. We will refer to $\delta \Pi_{ij}$ as the dissipative stresses. At first order in the gradient expansion $\delta \Pi_{ij}$ can be written as $\delta \Pi_{ij} = -\eta \sigma_{ij} - \zeta \delta_{ij} \langle \sigma \rangle$ with

$$\sigma_{ij} = \nabla_i u_j + \nabla_j u_i - \frac{2}{3} \delta_{ij} \langle \sigma \rangle, \quad \langle \sigma \rangle = \nabla \cdot \mathbf{u}. \quad (1.71)$$

The dissipative stresses are determined by two transport coefficients, the shear viscosity η and the bulk viscosity ζ . The energy current is given by

$$\mathbf{j}^\varepsilon = \mathbf{u} w + \delta \mathbf{j}^\varepsilon, \quad (1.72)$$

where $w = P + \mathcal{E}$ is the enthalpy. At leading order in the gradient expansion

$$\delta j_i^\varepsilon = u_j \delta \Pi_{ij} - \kappa \nabla_i T, \quad (1.73)$$

where κ is the thermal conductivity. The second law of thermodynamics implies that η , ζ and κ must be positive. The equation of motion for π at first order in gradients is known as the Navier-Stokes equation, and equ. (1.73) is Fourier's law of heat conduction.

It is sometimes useful to rewrite the fluid dynamic equations using the comoving derivatives $D_t = \partial_t + \mathbf{u} \cdot \nabla$. The equations are

$$D_t \rho = -\rho \nabla \cdot \mathbf{u}, \quad (1.74)$$

$$D_t u_i = -\frac{1}{\rho} \nabla_j (\delta_{ij} P + \delta \Pi_{ij}), \quad (1.75)$$

$$D_t \varepsilon = -\frac{1}{\rho} \nabla_i (u_i P + \delta j_i^\varepsilon), \quad (1.76)$$

where $\varepsilon = \mathcal{E}/\rho$ is the energy per mass. This is called the Lagrangian form of the equations, in contrast to the Eulerian form given above. The Eulerian form is more naturally implemented on a fixed space-time lattice, whereas the Lagrangian form lends itself to a discretization where the computational cell is dragged along with the fluid.

1.5.2 Computational fluid dynamics

The fluid dynamic equations form a set of partial differential equations (PDEs) that can be solved in a variety of ways. I will focus here on grid based methods. The main difficulties that a numerical method needs to address are: i) The existence of surfaces of discontinuity (shocks), ii) the need to implement global conservation laws exactly, even on a coarse lattice, iii) the existence of instabilities (turbulence), and the need to deal with solutions that involve many different length scales.

In the following I will discuss a numerical scheme that addresses these issues in a fairly efficient way, the PPM algorithm of Collella and Woodward [95], as implemented in the VH1 code by Blondin and Lufkin [96] and extended to viscous fluids in [97]. The first observation is that it is sufficient to construct a 1-d algorithm. Higher dimensional methods can be constructed by combining updates in different directions. Note that the coordinate system can be curvilinear, for example 3-d spherical or cylindrical coordinates, or the Milne coordinate system that is used for longitudinally expanding quark gluon plasmas.

The basic 1-d algorithm consists of a Lagrangian time step followed by a remap onto an Eulerian grid. I will denote the 1-d velocity by u and write the equation of mass conservation in terms of a mass variable m

$$\frac{\partial \tau}{\partial t} - \frac{\partial u}{\partial m} = 0, \quad (1.77)$$

where $\tau = \rho^{-1}$ and

$$m(r) = \int_{r_0}^r dr \rho(r). \quad (1.78)$$

Here, I restrict myself to flat coordinate systems. In curvilinear coordinates equ. (1.77) and (1.78) contain suitable volume factors. Equ. (1.77) is solved by

$$\frac{dr}{dt} = u(m(r), t), \quad (1.79)$$

which is the equation for the Lagrange coordinate. In terms of the mass coordinate $m(r)$ the momentum and energy equations are

$$\frac{\partial u}{\partial t} + \frac{\partial P}{\partial m} = 0, \quad (1.80)$$

$$\frac{\partial \varepsilon}{\partial t} + \frac{\partial (uP)}{\partial m} = 0, \quad (1.81)$$

where I have only written down the ideal contributions to the stress tensor and energy current. To put these equations on a grid I focus on the mass integrated quantities

$$U_j^n = \frac{1}{\Delta m_j} \int_{m_{j-1/2}}^{m_{j+1/2}} U(m, t^n) dm \quad (1.82)$$

where U is any of the hydrodynamic variables (τ, u, ε) , Δm_j is the mass contained in the cell j , and $m_{j+1/2} = \sum_k^j \Delta m_k$. We can now integrate the conservation laws (1.80, 1.77). The result is

$$u_j^{n+1} = u_j^n + \frac{\Delta t}{\Delta m_j} (\bar{P}_{j-1/2} - \bar{P}_{j+1/2}), \quad (1.83)$$

$$\varepsilon_j^{n+1} = \varepsilon_j^n + \frac{\Delta t}{\Delta m_j} (\bar{u}_{j-1/2} \bar{P}_{j-1/2} - \bar{u}_{j+1/2} \bar{P}_{j+1/2}), \quad (1.84)$$

where I have introduced the cell face averages $\bar{u}_{j\pm 1/2}$ and $\bar{P}_{j\pm 1/2}$. These quantities can be obtained by parabolic interpolation from the cell integrated values. The PPM scheme introduced in [95] uses a method for constructing cell face averages which conserves the cell integrated variables.

This scheme addresses the second issue mentioned above. The first issue, the existence of shocks, can be taken into account by refining the method for calculating the cell face averages. The observation is that one can make use of exact solution of the equations of fluid dynamics in the case of piecewise constant one-dimensional flows, known as the Riemann problem. We can view $\bar{u}_{j+1/2}$ and $\bar{P}_{j+1/2}$ as the solution of a Riemann problem with left state

u_j, P_j and right state u_{j+1}, P_{j+1} . The PPM code contains a simple iterative Riemann solver described in [95]. Using $\bar{u}_{j\pm 1/2}$ and $\bar{P}_{j\pm 1/2}$ the Lagrange step is given by:

```
do n = nmin-3, nmax+3

! density evolution. lagrangian code, so all we have to do is watch the
! change in the geometry.

r(n) = r(n) * ( dvol1(n) / dvol(n) )
r(n) = max(r(n), smallr)

! velocity evolution due to pressure acceleration and forces.

uold (n) = u(n)
u(n) = u(n) - dtbdm(n)*(pmid(n+1)-pmid(n))*0.5*(amid(n+1)+amid(n)) &
      + 0.5*dt*(fict0 (n)+fict1 (n))

! total energy evolution

e(n) = e(n) - dtbdm(n)*(amid(n+1)*upmid(n+1) - amid(n)*upmid(n))
q(n) = e(n) - 0.5*(u(n)**2+v(n)**2+w(n)**2)
p(n) = max(r(n)*q(n)*gamm, smallp)

enddo
```

Here, $r(n)$ is the density, $u(n)$ is the velocity, and $e(n)$ is the energy per mass. The transverse components of the velocity are $v(n), w(n)$. In cartesian coordinates the volume and area factors $dvol1(n), amid(n)$ are equal to unity, and the fictitious forces $fict(n)$ vanish.

After the Lagrange step the hydrodynamic variables have to be remapped onto a fixed Eulerian grid. This can be done using the parabolic interpolation mentioned above. The advantage of the remap step is that it is simple to change the grid resolution in the process. Finally, we have to specify the time step and grid resolution. The grid resolution is determined by the requirement that $(\Delta x)\nabla_x U \ll U$, where Δx is the cell size, and U is any of the hydrodynamic variables. Note that there is no need to worry about discontinuities, because shocks are captured by the Riemann solver. Also note that the PPM scheme has at least second order accuracy, so that relatively coarse grids can be used. The time step is determined by the Courant criterion $c\Delta x \leq \Delta t$, where c is the maximum of the speed of sound and the local flow velocity. This criterion ensures that the domain of dependence of any physical variable does not exceed the cell size.

In general, modern hydro codes are very fast and efficient. The main difficulty is that 3 + 1 dimensional simulations may require a lot of memory, and that some physical phenomena, such as turbulent convection and shock instabilities in supernovae, require very high resolution. One of the frontiers of numerical hydrodynamics is the problem of dealing with systems that transition from fluid dynamics to ballistic behavior at either early or late times, or systems in which the density varies by a very large factor. Problems of this type arise in the early and late time dynamics of heavy ion collisions, the dilute corona of cold atomic gases, and the transition from hydrodynamics to free streaming in the neutrino transport in a supernova explosions. Recent progress in this direction includes the development of the anisotropic hydrodynamics method [98–101], and applications of the lattice Boltzmann method to problems in nuclear and atomic physics [102, 103].

In the relativistic regime recent progress includes the development of stable and causal viscous fluid dynamics codes [92, 94]. The problem with a naive implementation of the relativistic Navier-Stokes equation derived by Landau is that viscous stresses are determined by the instantaneous value of the shear strain $\nabla_i u_j$. This leads to acausal propagation of shear waves and possible instabilities. This is not a fundamental problem with fluid dynamics. Acausal behavior occurs in the regime of high wave numbers in which fluid dynamics is not expected to be reliable. However, high wave number instabilities prohibit numerical implementations. The solution is to go to next order in the gradient expansion, which includes the finite relaxation time of viscous stresses. In practice, second order fluid dynamics codes are usually based on the idea of transient fluid dynamics. In this method, the shear stresses $\delta\Pi_{ij}$ are promoted to fluid dynamic variables, which satisfy separate fluid dynamic equations, see [92, 94].

1.5.3 Kinetic theory

Fluid dynamics is based on the assumption of local thermal equilibrium and requires the mean free path to be small compared to the characteristic scales of the problem. When this condition is not satisfied a more microscopic approach to the non-equilibrium problem is required. The simplest method of this type is kinetic theory, which is based on the existence of well defined quasi-particles. This implies, in particular, that the width of a quasi-particle has to be small compared to its energy. In this case we can define the phase space density $f(\mathbf{x}, \mathbf{p}, t)$ of quasi-particles. In general, there can be many different kinds of quasi-particles, labeled by their spin, charge, and other quantum numbers. The phase space distribution determines the conserved densities that enter the hydrodynamic description. For example, the mass density is given by

$$\rho(\mathbf{x}, t) = \int d\Gamma m f(\mathbf{x}, \mathbf{p}, t), \quad (1.85)$$

where $d\Gamma = d^3p/(2\pi)^3$. The momentum density is

$$\pi(\mathbf{x}, t) = \int d\Gamma m v_p f(\mathbf{x}, \mathbf{p}, t), \quad (1.86)$$

where $v_p = \nabla_p E_p$ is the quasi-particle velocity and E_p is the quasi-particle energy. In general, the quasi-particle energy can be a functional of the phase distribution $f(\mathbf{x}, \mathbf{p}, t)$. This takes into account possible in-medium modifications of particle properties. If E_p is a functional of $f(\mathbf{x}, \mathbf{p}, t)$ then the total energy of the system is not just given by the integral of $E_p f(\mathbf{x}, \mathbf{p}, t)$. Instead, we must construct an energy density functional $\mathcal{E}[f]$ that satisfies [104]

$$E_p = \frac{\delta \mathcal{E}}{\delta f_p}. \quad (1.87)$$

The equation of motion for the distribution function is the Boltzmann equation

$$(\partial_t + \mathbf{v} \cdot \nabla_x - \mathbf{F} \cdot \nabla_p) f(\mathbf{x}, \mathbf{p}, t) = C[f], \quad (1.88)$$

where $\mathbf{F} = -\nabla_x E_p$ is a force, and $C[f_p]$ is the collision term. For dilute systems the collision term is dominated by binary scattering and

$$C[f_p] = - \prod_{i=2,3,4} \left(\int d\Gamma_i \right) w(1,2;3,4) (f_1 f_2 - f_3 f_4), \quad (1.89)$$

where $f_i = f(\mathbf{x}, \mathbf{p}_i, t)$. The transition rate is given by

$$w(1,2;3,4) = (2\pi)^4 \delta\left(\sum_i E_i\right) \delta\left(\sum_i \mathbf{p}_i\right) |\mathcal{A}|^2, \quad (1.90)$$

where \mathcal{A} is the scattering amplitude. For non-relativistic s -wave scattering $\mathcal{A} = 4\pi a/m$, where a is the scattering length.

The Boltzmann equation is a 6+1 dimensional partial integro-differential equation, and direct methods of integration, similar to those used in computational fluid dynamics, are impractical. Standard methods for solving the Boltzmann equation rely on sampling phase space using Monte Carlo methods. In nuclear physics the test particle method for solving the Boltzmann equation was popularized by Bertsch and Das Gupta [105]. Below, I will present a simple non-relativistic algorithm described by Lepers et al. [106].

The main idea is to represent the distribution as a sum of delta functions

$$f(\mathbf{x}, \mathbf{p}, t) = \frac{N}{N_t} \sum_{i=1}^{N_t} (2\pi)^3 \delta(\mathbf{p} - \mathbf{p}_i(t)) \delta(\mathbf{x} - \mathbf{x}_i(t)), \quad (1.91)$$

where N is the number of particles, the integral of $f(\mathbf{x}, \mathbf{p}, t)$ over phase space, and N_t is the number of test particles. In typical applications $N_t \gg N$, but if N is already very large it is possible to run simulations with $N_t < N$. Phase space averages can be computed as averages over test particles

$$\bar{F} = \frac{1}{N} \int d^3x \int d\Gamma f(\mathbf{x}, \mathbf{p}, t) F(\mathbf{x}, \mathbf{p}) = \frac{1}{N_t} \sum_{i=1}^{N_t} F(\mathbf{x}_i, \mathbf{p}_i). \quad (1.92)$$

In practice this requires some smoothing, and the delta functions are replaced by Gaussian distributions

$$\delta(\mathbf{p} - \mathbf{p}_i) \delta(\mathbf{x} - \mathbf{x}_i) \rightarrow g_{w_p}(\mathbf{p} - \mathbf{p}_i) g_{w_x}(\mathbf{x} - \mathbf{x}_i), \quad (1.93)$$

where $g_w(\mathbf{x})$ is a normalized Gaussian with width w . The widths w_x and w_p are chosen such that the delta function singularities are smoothed out, but physical structures of the distribution function $f(\mathbf{x}, \mathbf{p}, t)$ are preserved.

If there is no collision term the equation of motion for the distribution function is Hamilton's equation for the test particle positions and momenta

$$\frac{d\mathbf{x}_i}{dt} = \frac{\mathbf{p}_i}{m}, \quad \frac{d\mathbf{p}_i}{dt} = \mathbf{F}_i. \quad (1.94)$$

These equations can be solved with high accuracy using a staggered leapfrog algorithm

$$\mathbf{v}_i(t_{n+1/2}) = \mathbf{v}_i(t_n) + \mathbf{a}_i(t_n) \Delta t / 2, \quad (1.95)$$

$$\mathbf{r}_i(t_{n+1}) = \mathbf{r}_i(t_n) + \mathbf{v}_i(t_{n+1/2}) \Delta t, \quad (1.96)$$

$$\mathbf{v}_i(t_{n+1}) = \mathbf{v}_i(t_{n+1/2}) + \mathbf{a}_i(t_{n+1}) \Delta t / 2, \quad (1.97)$$

where $\mathbf{a}_i = \mathbf{F}_i/m$ is the acceleration of particle i , and $\Delta t = t_{n+1} - t_n$ is the time step of the algorithm. The size of the time step depends on the specific problem, but a good check is provided by monitoring conservation of energy.

The collision term is treated stochastically, by allowing the test particles to collide with the scaled cross section $\sigma_t = (N/N_t)\sigma$. To determine whether a collision occurs we go through all pairs of particles and compute the relative distance $\mathbf{r}_{ij} = \mathbf{r}_i - \mathbf{r}_j$ and velocity $\mathbf{v}_{ij} = \mathbf{v}_i - \mathbf{v}_j$. We then determine whether on the current trajectory the time of closest approach will be reached during the next time step. This happens if $t_{min} = t_n - \mathbf{r}_{ij} \cdot \mathbf{v}_{ij} / \mathbf{v}_{ij}^2$ satisfies $|t_{min} - t_n| \leq \Delta t / 2$. In that case we compute

$$r_{min}^2 = \mathbf{r}_{ij}^2 - \frac{(\mathbf{r}_{ij} \cdot \mathbf{v}_{ij})^2}{\mathbf{v}_{ij}^2} \quad (1.98)$$

and check if $\pi r_{min}^2 < \sigma_t$. If this condition is satisfied then the collision is allowed to take place. For an s -wave elastic collision we propagate the particles to t_{min} , randomize their relative velocity \mathbf{v}_{ij} , and then propagate them back to t_n . Higher partial wave amplitudes are easy to implement by randomizing \mathbf{v}_{ij} with suitable probability distributions. After all pairs have been checked we perform the velocity and position update in equ. (1.95-1.97).

There are a number of refinements that can be included. At low temperature Pauli-blocking has to be taken into account. This can be done by computing the phase space densities $f(\mathbf{r}_i, \mathbf{p}_i, t)$ for the collision products, and accepting the collision with probability $(1 - f_i)(1 - f_j)$. At higher energies relativistic effects are important. Relativistic effects in the particle propagation are easy to incorporate, but the treatment of the collision term is more subtle. The problem is that a finite collision cross section, treated geometrically, will lead to instantaneous interactions at a distance. Additional difficulties arise from the treatment of resonances, pair production and annihilation, n -body processes, etc. There are a number of codes on the market that address these issues, and that have been tuned against existing data on pp , pA and AA interactions in the relativistic regime. Examples include UrQMD [107], GiBUU [108], HSD [109], and others.

At high energies the initial pp collisions are very inelastic, and one has to rely on Monte Carlo generators developed in the high energy physics community. A possible alternative is to use a purely partonic kinetic theory that involves scattering between quark and gluon quasi-particles. There are some subtleties with this approach, having to do with the problem of how to include screening and damping of the exchanged gluons, soft gluon radiation, etc. I will not attempt to discuss these issues here, and I refer the reader to the original literature [110, 111].

1.5.4 Classical field theory

An interesting simplification occurs if the occupation numbers are large, $f \gg 1$. This is argued to happen for the gluons in the initial state of a heavy ion collision [112]. In this limit the classical kinetic theory is equivalent to a classical field theory [113]. Indeed, if the occupations numbers are non-perturbative, $f \gtrsim 1/g$, the kinetic theory no longer applies, and we have to rely on classical field theory. In general the classical action is not known, but in the weak coupling limit the bare QCD action can be used.

Classical QCD simulation have been used to study a number of issues, such as particle production from an overpopulated gluon field, and the possible approach to thermal equilibrium. Instabilities in the classical field evolution may play an important role in speeding up the equilibration process. Here, I will briefly describe a method for solving classical evolution equations on a space-time lattice, following the recent review [114].

In order to construct a Hamiltonian approach to lattice QCD I start from the Wilson action in Minkowski space with separate coupling constants β_0 and β_s in the temporal and spatial direction

$$S[U] = -\frac{\beta_0}{2N_c} \sum_x \sum_{i=1}^3 \text{Tr} \left(W_{0i}(x) + W_{0i}^\dagger(x) - 2 \right) + \frac{\beta_s}{2N_c} \sum_x \sum_{i < j} \text{Tr} \left(W_{ij}(x) + W_{ij}^\dagger(x) - 2 \right), \quad (1.99)$$

In the continuum limit, we expect

$$\beta_0 = \frac{2N_c a}{g^2 \Delta t}, \quad \beta_s = \frac{2N_c \Delta t}{g^2 a}. \quad (1.100)$$

where a and Δt are spatial and temporal lattice spacings. In order to construct a Hamiltonian we have to fix the gauge freedom of the theory. Here, I will use the temporal axial gauge, $A_0 = 0$. In this case the canonical variables are the spatial gauge potentials and the conjugate momenta are the electric fields. On the lattice the gauge $A_0 = 0$ corresponds to setting all temporal gauge links to the identity, $U_0(x) = 1$. The canonical variables are given by the spatial gauge links $U_j(x)$, and the conjugate momenta are the temporal plaquettes $W_{0j}(x)$. In the continuum limit

$$A_j^a(x) = \frac{2i}{ag} \text{Tr}[\lambda^a U_j(x)], \quad (1.101)$$

$$E_j^a(x) = \frac{2i}{ag\Delta t} \text{Tr}[\lambda^a W_{0j}(x)]. \quad (1.102)$$

Varying the action equ. (1.99) with respect to $U_j(x)$ gives an equation of motion for E_j

$$E_j^a(t + \Delta t, \mathbf{x}) = E_j^a(t, \mathbf{x}) + \frac{i\Delta t}{ga^3} \sum_k \left\{ \text{Tr} \left[\lambda^a U_j(x) U_k(x + \hat{j}) U_j^\dagger(x + \hat{k}) U_k^\dagger(x) \right] \right. \\ \left. + \text{Tr} \left[\lambda^a U_j(x) U_k^\dagger(x + \hat{j} - \hat{k}) U_j^\dagger(x - \hat{k}) U_k(x - \hat{k}) \right] \right\}. \quad (1.103)$$

We note that $E_j^a(t + \Delta t, \mathbf{x})$ is determined by the electric fields and the spatial gauge links at time t . Using equ. (1.102) and the electric field E_j^a at time $t + \Delta t$ we can compute the temporal plaquette $W_{0j}(x)$ at $t + \Delta t$. This result can be used to evolve the spacelike gauge links

$$U_j(t + \Delta t, \mathbf{x}) = W_{0j}(x) U_j(x). \quad (1.104)$$

Together, equ. (1.103) and equ. (1.104) describe a staggered leapfrog algorithm, similar to equ. (1.95-1.97) above. An important constraint on the numerical evolution is provided by Gauss law. Varying the lattice action with respect to U_0 before imposing temporal axial gauge gives

$$\sum_j \left[E_j^a(x) - U_j^\dagger(x - \hat{j}) E_j^a(x - \hat{j}) U_j(x - \hat{j}) \right] = 0. \quad (1.105)$$

This constraint is preserved by the evolution equations.

The classical field equations are exactly scale invariant and there is no dependence on the coupling constant g . Physical quantities, like the energy momentum tensor, explicitly depend on g . In practice classical field simulations require a model for the initial conditions and the corresponding coupling. The initial conditions are typically an ensemble of gauge fields distributed according to some distribution, for example an anisotropic Gaussian in momentum space. The anisotropy is assumed to be a consequence of the strong longitudinal expansion of the initial state of a heavy ion collision. Physical observables are determined by averages the evolved fields over the initial ensemble.

Note that a purely classical field evolution does not thermalize. A thermal ensemble of classical fields would satisfy the equipartition law, and the total energy would be dominated by modes near the lattice cutoff. This is the Rayleigh-Jeans UV catastrophe. However, classical field evolution has interesting non-thermal fixed points [115], which may play a role in thermalization.

The classical field framework has been extended in a variety of ways. One direction is the inclusion of quantum fluctuations on top of the classical field [116]. Another problem is the inclusion of modes that are not highly populated. In the hard thermal loop approximation one can show that hard modes can be described as colored particles interacting with the classical field corresponding to the soft modes [117]. The equations of motion for the colored particles are known as Wong's equations [118]. Numerical studies can be found in [119].

1.5.5 Nonequilibrium QCD: Holography

A new approach to quantum fields in and out of equilibrium is provided by the AdS/CFT correspondence [120–124]. The AdS/CFT correspondence is a holographic duality. It asserts that the dynamics of a quantum field theory defined on the boundary of a higher dimensional space is encoded in boundary correlation functions of a gravitational theory in the bulk. The correspondence is simplest if the boundary theory is strongly coupled and contains a large number N of degrees of freedom. In this case the bulk theory is simply classical Einstein gravity. The partition function of the boundary quantum field theory (QFT) is

$$Z_{QFT}[J_i] = \exp(-S[\phi_i|_{\partial M} = J_i]), \quad (1.106)$$

where J_i is a set of sources in the field theory, S is the gravitational action, ϕ_i is a dual set of fields in the gravitational theory, and ∂M is the boundary of AdS_5 . The fields ϕ_i satisfy classical equations of motions subject to boundary conditions on ∂M .

The original construction involves a black hole in AdS_5 and is dual to a relativistic fluid governed by a generalization of QCD known as $\mathcal{N} = 4$ super Yang-Mills theory. This theory is considered in the limit of a large number of colors N_c . The gravitational theory is Einstein gravity with additional matter fields that are not relevant here. The AdS_5 black hole metric is

$$ds^2 = \frac{(\pi T R_a)^2}{u} (-f(u) dt^2 + d\mathbf{x}^2) + \frac{R_a^2}{4u^2 f(u)} du^2, \quad (1.107)$$

where \mathbf{x}, t are Minkowski space coordinates, and u is a “radial” coordinate where $u = 1$ is the location of the black hole horizon and $u = 0$ is the boundary. T is the temperature, R_a is the AdS radius, and $f(u) = 1 - u^2$.

It is instructive to check that this metric does indeed provide a solution to the Einstein equations with a negative cosmological constant. This can be done using a simple Mathematica script. I begin by defining the metric and its inverse:

```
(* metric *)
(* ----- *)
n = 5;
coord = {t, x, y, z, u};
f[u_] := 1 - u^2
metric = DiagonalMatrix[{-f[u]/u*(Pi*T*Ra)^2, (Pi*T*Ra)^2/u, (Pi*T*Ra)^2/
  u, (Pi*T*Ra)^2/u, Ra^2/(4*u^2*f[u])}]
inversemetric = Simplify[Inverse[metric]]
```

From the metric I compute the Christoffel symbols

$$\Gamma_{\alpha\beta}^{\mu} = \frac{1}{2} g^{\mu\nu} (\partial_{\alpha} g_{\nu\beta} + \partial_{\beta} g_{\nu\alpha} - \partial_{\nu} g_{\alpha\beta}), \quad (1.108)$$

the Riemann tensor

$$R_{\nu\alpha\beta}^{\mu} = \partial_{\alpha} \Gamma_{\nu\beta}^{\mu} - \partial_{\beta} \Gamma_{\nu\alpha}^{\mu} + \Gamma_{\nu\beta}^{\rho} \Gamma_{\rho\alpha}^{\mu} - \Gamma_{\nu\alpha}^{\rho} \Gamma_{\rho\beta}^{\mu}, \quad (1.109)$$

the Ricci tensor $R_{\alpha\beta} = R^{\mu}_{\alpha\mu\beta}$, and the scalar curvature $R = R^{\mu}_{\mu}$. Finally, I compute the Einstein tensor $G_{\mu\nu} = R_{\mu\nu} - \frac{1}{2} g_{\mu\nu} R$.

```
(* Christoffel Symbols *)
(* ----- *)
affine := affine = Simplify[
```

```

Table[(1/2)*
  Sum[(inversemetric[[i, s]]*(D[metric[[s, j]], coord[[k]]] +
    D[metric[[s, k]], coord[[j]]] -
    D[metric[[j, k]], coord[[s]])), {s, 1, n}], {i, 1, n}, {j, 1,
  n}, {k, 1, n}]

(* Riemann Tensor *)
(* ----- *)
riemann := riemann = Simplify[Table[
  D[affine[[i, j, l]], coord[[k]]] -
  D[affine[[i, j, k]], coord[[l]]] +
  Sum[affine[[s, j, l]]*affine[[i, k, s]] -
    affine[[s, j, k]]*affine[[i, l, s]], {s, 1, n}], {i, 1, n}, {j,
  1, n}, {k, 1, n}, {l, 1, n}]

(* Ricci Tensor *)
(* ----- *)
ricci := ricci = Simplify[
  Table[Sum[riemann[[i, j, i, l]], {i, 1, n}], {j, 1, n}, {l, 1, n}]

(* scalar curvature *)
(* ----- *)
scalar = Simplify[
  Sum[inversemetric[[i, j]]*ricci[[i, j]], {i, 1, n}, {j, 1, n}]

(* Einstein tensor *)
(* ----- *)
einstein = Simplify[ricci - (1/2)*scalar*metric]

```

Now I can check the equation of motion, $G_{\mu\nu} = \frac{\Lambda}{2}g_{\mu\nu}$, where the cosmological constant is determined by the AdS radius R .

```

(* Field equation with cosmological constant *)
(* ----- *)
lam = 12/Ra^2;
Simplify[einstein - lam/2*metric]

```

In the boundary theory the metric couples to the stress tensor $\Pi_{\mu\nu}$. Correlation functions of the stress tensor can be found by linearizing the bulk action around the AdS₅ solution, $g_{\mu\nu} = g_{\mu\nu}^0 + \delta g_{\mu\nu}$. Small oscillations of the off-diagonal strain δg_x^y are particularly simple, because the equation of motion for $\phi \equiv g_x^y$ is that of a minimally coupled scalar

$$\frac{1}{\sqrt{-g}}\partial_\mu(\sqrt{-g}g^{\mu\nu}\partial_\nu\phi) = 0. \quad (1.110)$$

The wave equation can be obtained using the metric coefficients defined above.

```

(* \sqrt{-g} g^{\nu\mu} \partial_{\nu} \Phi(t, z, u) *)
(* ----- *)
SqrtG = Simplify[Sqrt[-Det[metric]], {Ra > 0, T > 0, u > 0}]
dnuPhi = Table[D[Phi[t, z, u], coord[[i]]], {i, 1, n}];
DnuPhi = SqrtG*inversemetric.dnuPhi;

```

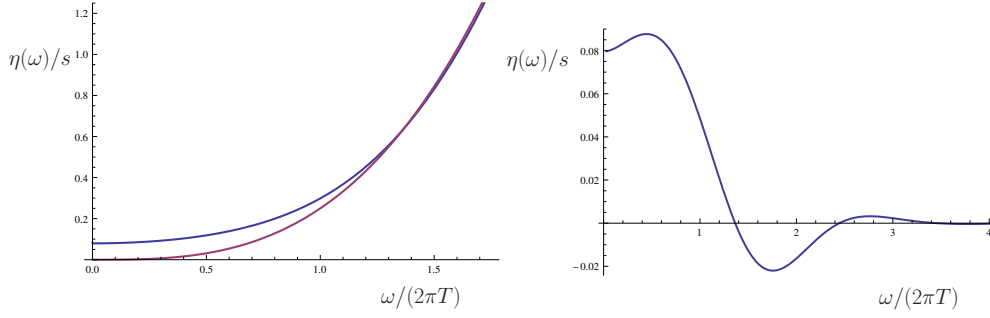


Fig. 1.5 Viscosity spectral function in a $\mathcal{N} = 4$ SUSY Yang Mills plasma. The spectral function is computed in the large N_c limit of a strongly coupled plasma using the AdS/CFT correspondence. The figure in the left panel shows $\eta(\omega)/s$ (blue) and the zero temperature counterpart $\eta_{T=0}(\omega)/s$ (red) as a function of ω . The figure in the right panel shows the finite temperature part $[\eta(\omega) - \eta_{T=0}(\omega)]/s$. The figures were generated using the script described below equ. (1.116).

```
(* Laplacian, up to factor \sqrt{-g} *)
(* ----- *)
DPhi = FullSimplify[Sum[D[DnuPhi[[nu]], coord[[nu]]], {nu, 1, n}]]

(* harmonic space and time dependence *)
(* ----- *)
DPhiS =
DPhi /. { D[Phi[t, z, u], {z, 2}] -> -k^2*fp,
          D[Phi[t, z, u], {t, 2}] -> -w^2*fp,
          D[Phi[t, z, u], {u, 2}] -> fpPP, D[Phi[t, z, u], {u, 1}] -> fpP}
```

In the case of harmonic dependence on the Minkowski coordinates $\delta g_x^y = \phi_k(u) e^{ikx - i\omega t}$ the fluctuations are governed by the wave equation

$$\phi_k''(u) - \frac{1+u^2}{uf(u)} \phi_k'(u) + \frac{\omega^2 - k^2 f(u)}{(2\pi T)^2 u f(u)^2} \phi_k(u) = 0. \quad (1.111)$$

This differential equation has two linearly independent solutions. The retarded correlation function corresponds to picking a solution that is purely infalling at the horizon [121]. The retarded correlation function $G_R(\omega, k)$ defined in equ. (1.60) is determined by inserting the solution into the Einstein-Hilbert action, and then computing the variation with respect to the boundary value of δg_x^y .

The infalling solution can be expressed as

$$\phi_k(u) = (1-u)^{-i\mathfrak{w}/2} F_k(u) \quad (1.112)$$

where $\mathfrak{w} = \omega/(2\pi T)$ and the first factor describes the near horizon behavior. The function $F_k(u)$ can be obtained as an expansion in \mathfrak{w} and $\mathfrak{k} = k/(2\pi T)$. At second order in $O(\mathfrak{w}$ and $\mathfrak{k})$ the solution is [125]

$$F_k(u) = 1 - \frac{i\mathfrak{w}}{2} \log\left(\frac{1+u}{2}\right) + \frac{\mathfrak{w}^2}{8} \left\{ \left[8 - \frac{8\mathfrak{k}^2}{\mathfrak{w}^2} + \log\left(\frac{1+u}{2}\right) \right] \log\left(\frac{1+u}{2}\right) - 4Li_2\left(\frac{1-u}{2}\right) \right\}. \quad (1.113)$$

In the opposite limit, $\mathfrak{w} \gg 1$, the wave equation can be solved using a WKB approximation [126]. For $\mathfrak{k} = 0$ the result is

$$\phi_k(u) = \pi w^2 \frac{u}{\sqrt{1-u^2}} [iJ_2(2w\sqrt{u}) - Y_2(2w\sqrt{u})]. \quad (1.114)$$

In the intermediate regime the wave equation can be solved numerically. A standard method is to start from the near horizon result given in equ. (1.112) and integrate outwards towards the boundary. The retarded correlation function is given by the variation of the boundary action with respect to the field. For this purpose we consider the quadratic part of the Einstein-Hilbert action and use the AdS/CFT correspondence to express Newton's constant in terms of gauge theory parameters. We find

$$S = -\frac{\pi^2 N^2 T^4}{8} \int du \int d^4x \frac{f(u)}{u} (\partial_u \phi)^2 + \dots \quad (1.115)$$

The boundary action follows after an integration by parts. The retarded Green function is determined by the second variational derivative with respect to the boundary value of the field [125, 127],

$$G_R(w, \mathfrak{k}) = -\frac{\pi^2 N^2 T^4}{4} \left[\frac{f(u) \partial_u \phi_k(u)}{u \phi_k(u)} \right]_{u \rightarrow 0}. \quad (1.116)$$

Finally, the spectral function is given by $\eta(\omega, k) = -\omega^{-1} \text{Im} G_R(\omega, k)$. Below is a short Mathematica script that determines the spectral function numerically.

```
(* equation of motion for minimally coupled scalar *)
(* with harmonic space and time dependence *)
(* ----- *)
f[u_] := 1 - u^2
EomPhi = phi'[u] - (1 + u^2)/(u f[u]) phi'[u]
+ (w^2 - q^2 f[u])/(u f[u]^2) phi[u]

(* boundary solution *)
(* ----- *)
phiHorizon[u_] := (1-u)^(-I*w/2)

(* numerically integrate from Horizon to boundary *)
(* ----- *)
SolPhi[omega_, qq_] := Block[{w = omega, q = qq},
  NDSolve[
    {0 == EomPhi,
     phi[epsH] == phiHorizon[epsH],
     phi'[epsH] == phiHorizon'[epsH]},
    phi[u],
    {u, epsB, epsH}][[1, 1, 2]]

(* retarded correlator from boundary action *)
(* ----- *)
Gret[omega_, qq_] := (f[u]/u D[solPhi[omega, qq], u]/solPhi[omega, qq] )
/. {u -> epsB}
```

The spectral function for $k = 0$ is shown in Fig. 1.5. This is an interesting result because it represent a systematic calculation of a real time observable in the strong coupling limit of a quantum field theory. As explained in Sect. 1.4.5 the corresponding lattice calculation is very difficult, and existing results are difficult to improve upon. We also note that the result is

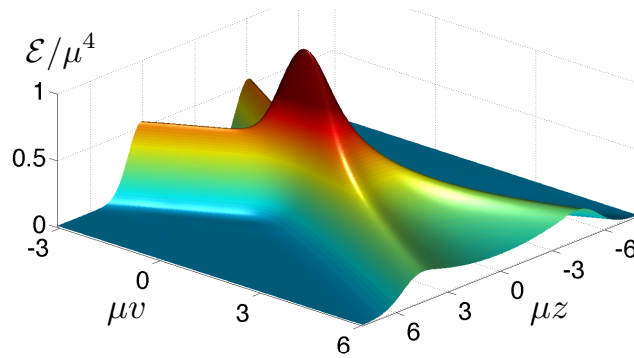


Fig. 1.6 Energy density of colliding shock waves in AdS_5 space [128]. The figure shows the energy density \mathcal{E}/μ^4 on the boundary of AdS_5 as a function of the time coordinate v and the longitudinal direction z . The shocks are infinitely extended in the transverse direction. The parameter μ sets the overall scale.

quite different from expectations at weak coupling. At weak coupling we expect the spectral function to show a narrow transport peak at zero energy [80].

So far we have only considered calculations very close to equilibrium, corresponding to small perturbations of the AdS_5 Schwarzschild solution. In order to address the problem of initial state dynamics and thermalization we have to consider initial conditions that mimic colliding nuclei. Recent work focuses on colliding shock waves in asymptotically AdS_5 spaces. In the strong coupling limit the evolution of the shock waves is a problem in numerical relativity. Special methods have been developed to deal with problems in AdS space [129]. These methods are quite different from the techniques employed in connection with black hole or neutron star mergers in asymptotically flat Minkowski space time. A typical result is shown in Fig. 1.6. The calculations demonstrate fast “hydrodynamization”, that means a rapid decay of non-hydrodynamic modes. At somewhat longer time scales thermal equilibration is achieved. This corresponds to the formation of an event horizon in the bulk. In general, it was realized that there is a fluid-gravity correspondence, an equivalence between dynamic space times containing a horizon and solutions of the Navier-Stokes equation [130]. This correspondence can be used to study, both analytically and numerically, difficult problems in fluid dynamics.

1.6 Outlook and acknowledgments

I hope this brief review provides a flavor of the breadth of computational problems that are related QCD. This includes many issues that are at the forefront of computational physics, like the sign problem in euclidean QCD at finite baryon density, and the challenge to extract real time correlation functions from the euclidean path integral. It also includes many problems that are of great interest to mathematicians. Both the Yang-Mills existence and mass gap as well as the Navier-Stokes existence and smoothness problems are among the Clay Millenium Prize problems [131, 132]. Interesting work on the Boltzmann equation was recently recognized with a Fields medal [133], and gradient flow plays an important role in the proof of the Poincare conjecture [134].

Acknowledgements The euclidean path integral simulation in quantum mechanics is described in [6], and the programs are available at <https://www.physics.ncsu.edu/schaefer/physics/>. A simple Z_2 lattice gauge code can be found in the Appendix. You should be able to extend this code to $SU(2)$ and $SU(3)$. Modern lattice QCD tools can be found on the chroma website <http://github.com/JeffersonLab/chroma>. The

VH1 hydro code is described in [96] and can be downloaded at <http://wonka.physics.ncsu.edu/pub/VH-1/>. Dissipative and anisotropic versions are available on request. There are a number of relativistic hydro codes on the web. An example is the VISHNU code [135] which is available at <https://u.osu.edu/vishnu/>. Both UrQMD <http://urqmd.org/> and GiBUU <https://gibuu.hepforge.org/> are also available online.

The mathematica notebooks in Sect. 1.5.5 are adapted from notebooks available on Jim Hartle's website <http://web.physics.ucsb.edu/~gravitybook/>. Much more sophisticated tensor packages are easily found on the web. The simple script for solving the wave equation in AdS_5 is adapted from a notebook written by Matthias Kaminski. A set of lecture notes and mathematica notebooks for solving the Einstein equations numerically on asymptotically AdS spaces can be found on Wilke van der Schee's website <https://sites.google.com/site/wilkevanderschee/ads-numeric>. T. S. work is supported by the US Department of Energy grant DE-FG02-03ER41260.

Appendix: Z_2 gauge theory

This is a simple Monte Carlo program for Z_2 gauge theory written by M. Creutz [136].

```

/* Z_2 lattice gauge simulation */
/* Michael Creutz <creutz@bnl.gov> */
/* http://thy.phy.bnl.gov/~creutz/z2.c */

#include <stdio.h>
#include <stdlib.h>
#include <math.h>

/* the lattice is of dimensions SIZE**4 */
#define SIZE 6
int link[SIZE][SIZE][SIZE][SIZE][4]; /* last index gives link direction */

/* utility functions */
void moveup(int x[],int d) {
    x[d]+=1;
    if (x[d]>=SIZE) x[d]-=SIZE;
    return;
}
void movedown(int x[],int d) {
    x[d]-=1;
    if (x[d]<0) x[d]+=SIZE;
    return;
}
void coldstart(){ /* set all links to unity */
    int x[4],d;
    for (x[0]=0;x[0]<SIZE;x[0]++)
        for (x[1]=0;x[1]<SIZE;x[1]++)
            for (x[2]=0;x[2]<SIZE;x[2]++)
                for (x[3]=0;x[3]<SIZE;x[3]++)
                    for (d=0;d<4;d++)
                        link[x[0]][x[1]][x[2]][x[3]][d]=1;
    return;
}
/* for a random start: call coldstart() and then update once at beta=0 */

/* do a Monte Carlo sweep; return energy */

```

```

double update(double beta){
  int x[4],d,dperp,staple,staplesum;
  double bplus,bminus,action=0.0;
  for (x[0]=0; x[0]<SIZE; x[0]++)
    for (x[1]=0; x[1]<SIZE; x[1]++)
      for (x[2]=0; x[2]<SIZE; x[2]++)
        for (x[3]=0; x[3]<SIZE; x[3]++)
          for (d=0; d<4; d++) {
            staplesum=0;
            for (dperp=0;dperp<4;dperp++){
              if (dperp!=d){
                /* move around thusly:
                   dperp      6—5
                   ^          | |
                   |          1—4
                   |          | |
                   ———> d    2—3  */
                /* plaquette 1234 */
                movedown(x,dperp);
                staple=link[x[0]][x[1]][x[2]][x[3]][dperp]
                  *link[x[0]][x[1]][x[2]][x[3]][d];
                moveup(x,d);
                staple*=link[x[0]][x[1]][x[2]][x[3]][dperp];
                moveup(x,dperp);
                staplesum+=staple;
                /* plaquette 1456 */
                staple=link[x[0]][x[1]][x[2]][x[3]][dperp];
                moveup(x,dperp);
                movedown(x,d);
                staple*=link[x[0]][x[1]][x[2]][x[3]][d];
                movedown(x,dperp);
                staple*=link[x[0]][x[1]][x[2]][x[3]][dperp];
                staplesum+=staple;
              }
            }
            /* calculate the Boltzmann weight */
            bplus=exp(beta*staplesum);
            bminus=1/bplus;
            bplus=bplus/(bplus+bminus);
            /* the heatbath algorithm */
            if ( drand48() < bplus ){
              link[x[0]][x[1]][x[2]][x[3]][d]=1;
              action+=staplesum;
            }
            else{
              link[x[0]][x[1]][x[2]][x[3]][d]=-1;
              action-=staplesum;
            }
          }
        }
      }
    }
  action /= (SIZE*SIZE*SIZE*SIZE*4*6);
  return 1.-action;
}

```

```
}

/*****
int main(){
    double beta, dbeta, action;
    srand48(1234L); /* initialize random number generator */
    /* do your experiment here; this example is a thermal cycle */
    dbeta=.01;
    coldstart();
    /* heat it up */
    for (beta=1; beta>0.0; beta-=dbeta){
        action=update(beta);
        printf("%g\t%g\n",beta,action);
    }
    printf("\n\n");
    /* cool it down */
    for (beta=0; beta<1.0; beta+=dbeta){
        action=update(beta);
        printf("%g\t%g\n",beta,action);
    }
    printf("\n\n");
    exit(0);
}
```

References

1. R.P. Feynman, A.R. Hibbs, *Quantum Mechanics and Path Integrals* (McGraw-Hill, 1965)
2. N. Metropolis, A.W. Rosenbluth, M.N. Rosenbluth, A.H. Teller, E. Teller, J. Chem. Phys. **21**, 1087 (1953). DOI 10.1063/1.1699114
3. M. Creutz, B. Freedman, Annals Phys. **132**, 427 (1981). DOI 10.1016/0003-4916(81)90074-9
4. E.V. Shuryak, O.V. Zhirov, Nucl. Phys. **B242**, 393 (1984). DOI 10.1016/0550-3213(84)90401-2
5. E.V. Shuryak, Nucl. Phys. **B302**, 621 (1988). DOI 10.1016/0550-3213(88)90191-5
6. T. Schäfer, Instantons and Monte Carlo methods in quantum mechanics (2004). ArXiv:hep-lat/0411010
7. M. Jarrell, J.E. Gubernatis, Phys. Rept. **269**, 133 (1996). DOI 10.1016/0370-1573(95)00074-7
8. M. Asakawa, T. Hatsuda, Y. Nakahara, Prog. Part. Nucl. Phys. **46**, 459 (2001). DOI 10.1016/S0146-6410(01)00150-8
9. C. Jarzynski, Physical Review Letters **78**, 2690 (1997). DOI 10.1103/PhysRevLett.78.2690
10. D.J. Gross, F. Wilczek, Phys.Rev.Lett. **30**, 1343 (1973). DOI 10.1103/PhysRevLett.30.1343
11. H.D. Politzer, Phys.Rev.Lett. **30**, 1346 (1973). DOI 10.1103/PhysRevLett.30.1346
12. S.R. Coleman, E.J. Weinberg, Phys.Rev. **D7**, 1888 (1973). DOI 10.1103/PhysRevD.7.1888
13. K. Nakamura, et al., J. Phys. **G37**, 075021 (2010). DOI 10.1088/0954-3899/37/7A/075021
14. M.G. Alford, A. Schmitt, K. Rajagopal, T. Schäfer, Rev. Mod. Phys. **80**, 1455 (2008). DOI 10.1103/RevModPhys.80.1455
15. A. Adams, L.D. Carr, T. Schäfer, P. Steinberg, J.E. Thomas, New J. Phys. **14**, 115009 (2012). DOI 10.1088/1367-2630/14/11/115009
16. P. Braun-Munzinger, V. Koch, T. Schäfer, J. Stachel, Phys. Rept. **621**, 76 (2016). DOI 10.1016/j.physrep.2015.12.003
17. M. Gell-Mann, R.J. Oakes, B. Renner, Phys. Rev. **175**, 2195 (1968). DOI 10.1103/PhysRev.175.2195
18. S.R. Coleman, E. Witten, Phys. Rev. Lett. **45**, 100 (1980). DOI 10.1103/PhysRevLett.45.100
19. G. 't Hooft, NATO Sci. Ser. B **59**, 135 (1980)
20. E.V. Shuryak, Sov. Phys. JETP **47**, 212 (1978). [Zh. Eksp. Teor. Fiz.74,408(1978)]
21. E.V. Shuryak, Phys. Lett. **B78**, 150 (1978). DOI 10.1016/0370-2693(78)90370-2. [Yad. Fiz.28,796(1978)]
22. A.D. Linde, Phys. Lett. **B96**, 289 (1980). DOI 10.1016/0370-2693(80)90769-8
23. R.D. Pisarski, F. Wilczek, Phys. Rev. **D29**, 338 (1984). DOI 10.1103/PhysRevD.29.338
24. Y. Aoki, G. Endrodi, Z. Fodor, S.D. Katz, K.K. Szabo, Nature **443**, 675 (2006). DOI 10.1038/nature05120
25. A. Bazavov, et al., Phys. Rev. **D85**, 054503 (2012). DOI 10.1103/PhysRevD.85.054503
26. Y. Aoki, Z. Fodor, S.D. Katz, K.K. Szabo, Phys. Lett. **B643**, 46 (2006). DOI 10.1016/j.physletb.2006.10.021
27. Y. Aoki, S. Borsanyi, S. Durr, Z. Fodor, S.D. Katz, S. Krieg, K.K. Szabo, JHEP **06**, 088 (2009). DOI 10.1088/1126-6708/2009/06/088
28. A. Bazavov, et al., Phys. Rev. **D90**(9), 094503 (2014). DOI 10.1103/PhysRevD.90.094503
29. M.A. Stephanov, Prog. Theor. Phys. Suppl. **153**, 139 (2004)
30. Z. Fodor, S.D. Katz, JHEP **03**, 014 (2002)
31. C. Allton, S. Ejiri, S. Hands, O. Kaczmarek, F. Karsch, et al., Phys.Rev. **D66**, 074507 (2002). DOI 10.1103/PhysRevD.66.074507
32. F. Karsch, C.R. Allton, S. Ejiri, S.J. Hands, O. Kaczmarek, E. Laermann, C. Schmidt, Nucl. Phys. Proc. Suppl. **129**, 614 (2004). DOI 10.1016/S0920-5632(03)02659-8. [614(2003)]
33. Z. Fodor, S. Katz, JHEP **0404**, 050 (2004). DOI 10.1088/1126-6708/2004/04/050
34. R.V. Gavai, S. Gupta, Phys. Rev. **D78**, 114503 (2008). DOI 10.1103/PhysRevD.78.114503
35. S. Datta, R.V. Gavai, S. Gupta, Nucl. Phys. **A904-905**, 883c (2013). DOI 10.1016/j.nuclphysa.2013.02.156
36. P. de Forcrand, O. Philipsen, Phys. Rev. Lett. **105**, 152001 (2010). DOI 10.1103/PhysRevLett.105.152001
37. M.A. Stephanov, K. Rajagopal, E.V. Shuryak, Phys. Rev. Lett. **81**, 4816 (1998)
38. G. Sauer, H. Chandra, U. Mosel, Nucl. Phys. **A264**, 221 (1976). DOI 10.1016/0375-9474(76)90429-2
39. J. Pochoodzalla, et al., Phys. Rev. Lett. **75**, 1040 (1995). DOI 10.1103/PhysRevLett.75.1040
40. J.B. Elliott, P.T. Lake, L.G. Moretto, L. Phair, Phys. Rev. **C87**(5), 054622 (2013). DOI 10.1103/PhysRevC.87.054622
41. M.G. Alford, K. Rajagopal, F. Wilczek, Nucl. Phys. **B537**, 443 (1999). DOI 10.1016/S0550-3213(98)00668-3
42. T. Schäfer, Nucl. Phys. **B575**, 269 (2000). DOI 10.1016/S0550-3213(00)00063-8
43. T. Schäfer, F. Wilczek, Phys. Rev. Lett. **82**, 3956 (1999). DOI 10.1103/PhysRevLett.82.3956
44. T. Hatsuda, M. Tachibana, N. Yamamoto, G. Baym, Phys. Rev. Lett. **97**, 122001 (2006). DOI 10.1103/PhysRevLett.97.122001
45. M. Creutz, *Quarks, Gluons, and Lattices* (Cambridge University Press, 1983)
46. I. Montvay, G. Münster, *Quantum Fields on a Lattice* (Cambridge University Press, 1994)
47. J. Smit, *Introduction to Quantum Fields on a Lattice* (Cambridge University Press, 2002)

48. C. Gattringer, C.B. Lang, *Quantum Chromodynamics on the Lattice* (Springer, 2009)
49. H.W. Lin, H.B. Meyer, *Lattice QCD for Nuclear Physics* (Springer, 2014)
50. Z. Fodor, S.D. Katz, The Phase diagram of quantum chromodynamics (2009). ArXiv:0908.3341
51. H.T. Ding, F. Karsch, S. Mukherjee, Thermodynamics of strong-interaction matter from Lattice QCD (2015). ArXiv:1504.05274
52. K.G. Wilson, Phys. Rev. **D10**, 2445 (1974). DOI 10.1103/PhysRevD.10.2445. [45(1974)]
53. F. Mezzadri, How to generate random matrices from the classical compact groups (2006). ArXiv:math-ph/0609050
54. A. Hasenfratz, P. Hasenfratz, Phys. Lett. **B93**, 165 (1980). DOI 10.1016/0370-2693(80)90118-5. [241(1980)]
55. G.P. Lepage, in *Strong interactions at low and intermediate energies. Proceedings, 13th Annual Hampton University Graduate Studies, HUGS'98, Newport News, USA, May 26-June 12, 1998* (1998), pp. 49–90
56. U. Wolff, Phys. Rev. Lett. **62**, 361 (1989). DOI 10.1103/PhysRevLett.62.361
57. J.B. Kogut, L. Susskind, Phys. Rev. **D11**, 395 (1975). DOI 10.1103/PhysRevD.11.395
58. D.B. Kaplan, Phys. Lett. **B288**, 342 (1992). DOI 10.1016/0370-2693(92)91112-M
59. H. Neuberger, Phys. Lett. **B417**, 141 (1998). DOI 10.1016/S0370-2693(97)01368-3
60. M. Luscher, in *Modern perspectives in lattice QCD: Quantum field theory and high performance computing. Proceedings, International School, 93rd Session, Les Houches, France, August 3-28, 2009* (2010), pp. 331–399
61. E. Endress, C. Pena, K. Sivalingam, Comput. Phys. Commun. **195**, 35 (2015). DOI 10.1016/j.cpc.2015.04.017
62. V. Dick, F. Karsch, E. Laermann, S. Mukherjee, S. Sharma, Phys. Rev. **D91**(9), 094504 (2015). DOI 10.1103/PhysRevD.91.094504
63. M. Teper, Phys. Lett. **B171**, 86 (1986). DOI 10.1016/0370-2693(86)91004-X
64. M. Lüscher, JHEP **08**, 071 (2010). DOI 10.1007/JHEP08(2010)071, 10.1007/JHEP03(2014)092. [Erratum: JHEP03,092(2014)]
65. A.A. Belavin, A.M. Polyakov, A.S. Schwartz, Yu.S. Tyupkin, Phys. Lett. **B59**, 85 (1975). DOI 10.1016/0370-2693(75)90163-X
66. T. Schäfer, E.V. Shuryak, Rev. Mod. Phys. **70**, 323 (1998). DOI 10.1103/RevModPhys.70.323
67. L. Del Debbio, L. Giusti, C. Pica, Phys. Rev. Lett. **94**, 032003 (2005). DOI 10.1103/PhysRevLett.94.032003
68. M. Ce, C. Consonni, G.P. Engel, L. Giusti, PoS **LATTICE2014**, 353 (2014)
69. E. Poppitz, T. Schäfer, M. Ünsal, JHEP **03**, 087 (2013). DOI 10.1007/JHEP03(2013)087
70. T. Banks, A. Casher, Nucl. Phys. **B169**, 103 (1980). DOI 10.1016/0550-3213(80)90255-2
71. P.H. Ginsparg, K.G. Wilson, Phys. Rev. **D25**, 2649 (1982). DOI 10.1103/PhysRevD.25.2649
72. A. Cherman, T. Schäfer, M. Ünsal, Chiral Lagrangian from Duality and Monopole Operators in Compactified QCD (2016). ArXiv:1604.06108
73. S.R. Beane, P.F. Bedaque, A. Parreno, M.J. Savage, Phys. Lett. **B585**, 106 (2004). DOI 10.1016/j.physletb.2004.02.007
74. M. Cristoforetti, F. Di Renzo, L. Scorzato, Phys. Rev. **D86**, 074506 (2012). DOI 10.1103/PhysRevD.86.074506
75. G. Aarts, L. Bongiovanni, E. Seiler, D. Sexty, JHEP **10**, 159 (2014). DOI 10.1007/JHEP10(2014)159
76. G. Aarts, E. Seiler, I.O. Stamatescu, Phys. Rev. **D81**, 054508 (2010). DOI 10.1103/PhysRevD.81.054508
77. D. Sexty, Phys. Lett. **B729**, 108 (2014). DOI 10.1016/j.physletb.2014.01.019
78. T. Kloiber, C. Gattringer, PoS **LATTICE2013**, 206 (2014)
79. T. Schäfer, D. Teaney, Rept. Prog. Phys. **72**, 126001 (2009). DOI 10.1088/0034-4885/72/12/126001
80. T. Schäfer, Ann. Rev. Nucl. Part. Sci. **64**, 125 (2014). DOI 10.1146/annurev-nucl-102313-025439
81. F. Karsch, H.W. Wyld, Phys. Rev. **D35**, 2518 (1987). DOI 10.1103/PhysRevD.35.2518
82. H.B. Meyer, Phys. Rev. **D76**, 101701 (2007). DOI 10.1103/PhysRevD.76.101701
83. H.B. Meyer, Phys. Rev. Lett. **100**, 162001 (2008). DOI 10.1103/PhysRevLett.100.162001
84. S. Sakai, A. Nakamura, PoS **LAT2007**, 221 (2007). DOI 10.1063/1.2729742. [AIP Conf. Proc.893,5(2007)]
85. G. Aarts, C. Allton, J. Foley, S. Hands, S. Kim, Phys. Rev. Lett. **99**, 022002 (2007). DOI 10.1103/PhysRevLett.99.022002
86. G. Aarts, PoS **LAT2007**, 001 (2007)
87. G. Aarts, C. Allton, J. Foley, S. Hands, S. Kim, Nucl. Phys. **A785**, 202 (2007). DOI 10.1016/j.nuclphysa.2006.11.148
88. H.B. Meyer, JHEP **08**, 031 (2008). DOI 10.1088/1126-6708/2008/08/031
89. P. Romatschke, D.T. Son, Phys. Rev. **D80**, 065021 (2009). DOI 10.1103/PhysRevD.80.065021
90. P.B. Arnold, G.D. Moore, L.G. Yaffe, JHEP **11**, 001 (2000). DOI 10.1088/1126-6708/2000/11/001
91. P. Kovtun, D.T. Son, A.O. Starinets, Phys. Rev. Lett. **94**, 111601 (2005). DOI 10.1103/PhysRevLett.94.111601

92. P. Romatschke, *Int. J. Mod. Phys.* **E19**, 1 (2010). DOI 10.1142/S0218301310014613
93. L. Rezzolla, O. Zanotti, *Relativistic Hydrodynamics* (Oxford University Press, 2013)
94. S. Jeon, U. Heinz, *Int. J. Mod. Phys.* **E24**(10), 1530010 (2015). DOI 10.1142/S0218301315300106
95. P. Colella, P.R. Woodward, *J. Comp. Phys.* **54**, 174 (1984)
96. J.M. Blondin, E.A. Lufkin, *Astrophys. J. Supp. Ser.* **88**, 589 (1993)
97. T. Schäfer, *Phys. Rev.* **A82**, 063629 (2010). DOI 10.1103/PhysRevA.82.063629
98. W. Florkowski, R. Ryblewski, *Phys. Rev.* **C83**, 034907 (2011). DOI 10.1103/PhysRevC.83.034907
99. M. Martinez, M. Strickland, *Nucl. Phys.* **A848**, 183 (2010). DOI 10.1016/j.nuclphysa.2010.08.011
100. M. Bluhm, T. Schäfer, *Phys. Rev.* **A92**(4), 043602 (2015). DOI 10.1103/PhysRevA.92.043602
101. M. Bluhm, T. Schäfer, *Phys. Rev. Lett.* **116**(11), 115301 (2016). DOI 10.1103/PhysRevLett.116.115301
102. P. Romatschke, M. Mendoza, S. Succi, *Phys. Rev.* **C84**, 034903 (2011). DOI 10.1103/PhysRevC.84.034903
103. J. Brewer, M. Mendoza, R.E. Young, P. Romatschke, *Phys. Rev.* **A93**(1), 013618 (2016). DOI 10.1103/PhysRevA.93.013618
104. L.P. Kadanoff, G. Baym, *Quantum Statistical Mechanics* (W. A. Benjamin, 1962)
105. G.F. Bertsch, S. Das Gupta, *Phys. Rept.* **160**, 189 (1988). DOI 10.1016/0370-1573(88)90170-6
106. T. Lepers, D. Davesne, S. Chiacchiera, M. Urban, *Phys. Rev.* **A82**, 023609 (2010). DOI 10.1103/PhysRevA.82.023609
107. S.A. Bass, et al., *Prog. Part. Nucl. Phys.* **41**, 255 (1998). DOI 10.1016/S0146-6410(98)00058-1. [*Prog. Part. Nucl. Phys.*41,225(1998)]
108. O. Buss, T. Gaitanos, K. Gallmeister, H. van Hees, M. Kaskulov, O. Lalakulich, A.B. Larionov, T. Leitner, J. Weil, U. Mosel, *Phys. Rept.* **512**, 1 (2012). DOI 10.1016/j.physrep.2011.12.001
109. W. Ehehalt, W. Cassing, *Nucl. Phys.* **A602**, 449 (1996). DOI 10.1016/0375-9474(96)00097-8
110. K. Geiger, B. Muller, *Nucl. Phys.* **B369**, 600 (1992). DOI 10.1016/0550-3213(92)90280-O
111. Z. Xu, C. Greiner, *Phys. Rev.* **C71**, 064901 (2005). DOI 10.1103/PhysRevC.71.064901
112. L.D. McLerran, R. Venugopalan, *Phys. Rev.* **D49**, 2233 (1994). DOI 10.1103/PhysRevD.49.2233
113. A.H. Mueller, D.T. Son, *Phys. Lett.* **B582**, 279 (2004). DOI 10.1016/j.physletb.2003.12.047
114. S. Mrowczynski, B. Schenke, M. Strickland, (2016)
115. J. Berges, A. Rothkopf, J. Schmidt, *Phys. Rev. Lett.* **101**, 041603 (2008). DOI 10.1103/PhysRevLett.101.041603
116. K. Dusling, T. Epelbaum, F. Gelis, R. Venugopalan, *Nucl. Phys.* **A850**, 69 (2011). DOI 10.1016/j.nuclphysa.2010.11.009
117. D.F. Litim, C. Manuel, *Phys. Rept.* **364**, 451 (2002). DOI 10.1016/S0370-1573(02)00015-7
118. S.K. Wong, *Nuovo Cim.* **A65**, 689 (1970). DOI 10.1007/BF02892134
119. C.R. Hu, B. Muller, *Phys. Lett.* **B409**, 377 (1997). DOI 10.1016/S0370-2693(97)00851-4
120. J.M. Maldacena, *Int. J. Theor. Phys.* **38**, 1113 (1999). DOI 10.1023/A:1026654312961. [*Adv. Theor. Math. Phys.*2,231(1998)]
121. D.T. Son, A.O. Starinets, *Ann. Rev. Nucl. Part. Sci.* **57**, 95 (2007). DOI 10.1146/annurev.nucl.57.090506.123120
122. S.S. Gubser, A. Karch, *Ann. Rev. Nucl. Part. Sci.* **59**, 145 (2009). DOI 10.1146/annurev.nucl.010909.083602
123. J. Casalderrey-Solana, H. Liu, D. Mateos, K. Rajagopal, U.A. Wiedemann, (2011)
124. O. DeWolfe, S.S. Gubser, C. Rosen, D. Teaney, *Prog. Part. Nucl. Phys.* **75**, 86 (2014). DOI 10.1016/j.pnpnp.2013.11.001
125. G. Policastro, D.T. Son, A.O. Starinets, *JHEP* **09**, 043 (2002). DOI 10.1088/1126-6708/2002/09/043
126. D. Teaney, *Phys. Rev.* **D74**, 045025 (2006). DOI 10.1103/PhysRevD.74.045025
127. D.T. Son, A.O. Starinets, *JHEP* **03**, 052 (2006). DOI 10.1088/1126-6708/2006/03/052
128. P.M. Chesler, L.G. Yaffe, *Phys. Rev. Lett.* **106**, 021601 (2011). DOI 10.1103/PhysRevLett.106.021601
129. P.M. Chesler, L.G. Yaffe, *JHEP* **07**, 086 (2014). DOI 10.1007/JHEP07(2014)086
130. M. Rangamani, *Class. Quant. Grav.* **26**, 224003 (2009). DOI 10.1088/0264-9381/26/22/224003
131. A. Jaffe, E. Witten, *Quantum Yang Mills Theory*, Official Description of Millenium Prize Problems (2000). www.claymath.org
132. C. Fefferman, *Existence and smoothness of the Navier-Stokes Equation*, Official Description of Millenium Prize Problems (2000). www.claymath.org
133. C. Mouhot, C. Villani, *Acta Mathematica* **207**, 29 (2011). DOI 10.1007/s11511-011-0068-9
134. G. Perelman, *The entropy formula for the Ricci flow and its geometric applications* (2002). [ArXiv:math/0211159](https://arxiv.org/abs/math/0211159) [math.DG]
135. C. Shen, Z. Qiu, H. Song, J. Bernhard, S. Bass, U. Heinz, *Comput. Phys. Commun.* **199**, 61 (2016). DOI 10.1016/j.cpc.2015.08.039
136. M. Creutz, *Computers in Science & Engineering* **March/April 2004**, 80 (2004)